

# Investigations to Decrease Losses in Magnetohydrodynamic (MHD) Generators

(SUIPR Report No. 454)

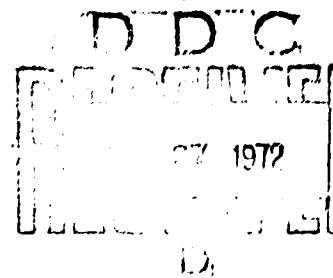
R. H. Eustis, C. H. Kruger, M. Mitchner, et al

Stanford University

Technical Report AFAPL-TR-72-15

February 1972

Approved for public release,  
distribution unlimited.



Air Force Aero Propulsion Laboratory  
Air Force Systems Command  
Wright-Patterson Air Force Base, Ohio 45433

Reproduced by  
NATIONAL TECHNICAL  
INFORMATION SERVICE  
Springfield, Va. 22151

HIGH TEMPERATURE GASDYNAMICS LABORATORY  
MECHANICAL ENGINEERING DEPARTMENT

STANFORD UNIVERSITY ■ STANFORD, CALIFORNIA

AD 740 560  
AD 740 560  
AD 740 560

## NOTICE

When Government drawings, specifications, or other data are used for any purpose other than in connection with a definitely related Government procurement operation, the United States Government thereby incurs no responsibility nor any obligation whatsoever; and the fact that the government may have formulated, furnished, or in any way supplied the said drawings, specifications, or other data, is not to be regarded by implication or otherwise as in any manner licensing the holder or any other person or corporation, or conveying any rights or permission to manufacture, use, or sell any patented invention that may in any way be related thereto.

COPIES IN

201	WHITE	<input checked="checked" type="checkbox"/>
	DOVE GREEN	<input type="checkbox"/>
		<input type="checkbox"/>

A

Copies of this report should not be returned unless return is required by security considerations, contractual obligations, or notice on a specific document.

UNCLASSIFIED

Security Classification

## DOCUMENT CONTROL DATA - R &amp; D

(Security classification of title, body of abstract and indexing annotation must be entered when the overall report is classified)

1. ORIGINATING ACTIVITY (Corporate author)

Stanford University  
Department of Mechanical Engineering  
Stanford, California 94305

2a. REPORT SECURITY CLASSIFICATION

UNCLASSIFIED

2b. GROUP

3. REPORT TITLE

INVESTIGATIONS TO DECREASE LOSSES IN MHD GENERATORS

4. DESCRIPTIVE NOTES (Type of report and inclusive dates)

Final Technical Report - 9.15/68 - 7/31.71

5. AUTHOR(S) (First name, middle initial, last name)

Robert H. Eustis, Charles H. Kruger, Morton Mitchner,

6. REPORT DATE

February 1972

7a. TOTAL NO. OF PAGES

73

7b. NO. OF REFS

11

8a. CONTRACT OR GRANT NO.

AF F33615-69-C-1171

b. PROJECT NO.

3145

c. Task No.

314526

d.

9a. ORIGINATOR'S REPORT NUMBER(S)

SU-IPR #454

9b. OTHER REPORT NO(S) (Any other numbers that may be assigned this report)

AFAPL-TR-72-15

10. DISTRIBUTION STATEMENT

Approved for public release; distribution unlimited

11. SUPPLEMENTARY NOTES

12. SPONSORING MILITARY ACTIVITY

Air Force Aero Propulsion Laboratory  
Wright-Patterson Air Force Base  
Ohio 45433

13. ABSTRACT

The research program described in this Final Report has included work on boundary layer studies, current distribution and current leakage in MHD generators, and boundary layer diagnostics. A computer program which has been used successfully to calculate conventional turbulent boundary layers has been modified by adding the MHD terms in the momentum and energy equations. This modified program has been coupled to a one-dimensional core-flow program to give boundary layer parameters in an MHD generator. Experiments were made in arc-heated argon with small additions of  $N_2$  and  $CO_2$  to delineate the effect of these components on electrode voltage drops. The effect was larger than could be predicted from ambipolar diffusion theory. Analysis and experiments made with electrodes of several sizes showed the important influence of boundary layer and electrode temperatures. Because the boundary layer temperature is coupled to the electrode temperature, small cold electrodes performed better than large cold electrodes in the Stanford MHD generator.

Current patterns in conducting wall generators were measured and showed good agreement with theoretical predictions for the anode. The surface-sheath voltage drop was responsible for less good agreement at the cathode. It was shown that a large fraction of the current entered the sidewalls of a conducting wall generator. Experiments also indicated that Faraday electrodes which included part of the sidewall gave a greater power output than conventional flat electrodes. Axial current leakage in the Hall direction was calculated and measured in a simulated MHD generator using argon with up to 20%  $N_2$  diluent. Agreement between experiment and theory was satisfactory. For combustion gases with diffuse currents the theory predicts larger Hall voltages before breakdown than have been observed in practice. The Hall voltage limitation is believed

DD FORM 1473

1 NOV 63

UNCLASSIFIED

Security Classification

KEY WORDS	LINK A		LINK B		LINK C	
	ROLE	WT	ROLE	WT	ROLE	WT
Magnetohydrodynamics Boundary Layers Spectroscopic Diagnostics						
<u>Abstract (Cont.)</u> associated with arcing phenomena. A new method which uses Faraday splitting of laser modes is suggested for the measurement of electron concentration in the boundary layer. A laser doppler velocimeter and its applications to boundary layer velocity measurements in the Stanford generator is described.						

AFAPL-TR-72-15

INVESTIGATIONS TO DECREASE LOSSES IN MAGNETOHYDRODYNAMIC (MHD) GENERATORS  
(SUIPR Report No. 454)

R. H. Eustis, C. H. Kruger, M. Mitchner, et al  
Stanford University

TECHNICAL REPORT AFAPL-TR-72-15

February 1972

Approved for public release,  
distribution unlimited

Air Force Aero Propulsion Laboratory  
Air Force Systems Command  
Wright-Patterson Air Force Base, Ohio 45433

## FOREWORD

The research described in the Final Report was performed in the High Temperature Gasdynamics Laboratory of Stanford University, Stanford, California, under contract AF F33615-69-C-1171, project number 3i45, task number 3i4526. The program was supported by the Air Force Aero Propulsion Laboratory, Wright Patterson Air Force Base, Ohio. Mr. Robert F. Cooper and Mr. Paul Lindquist, POP-2, served as technical managers. This report covers the period 9/15/68 to 7/31/71 and was submitted on January 24, 1972.

The authors would like to point out the very important contributions made by Stanford graduate students during this research program. In particular Mr. S. J. Morris was responsible for the computer program described in Section 2.1, Mr. G. A. DuBro made the measurements of Section 2.2, and Dr. E. S. Rubin performed the calculations and experiments presented in Section 2.3. Mr. R. M. Cima and Mr. K. E. Berry assisted with the current distribution work described in Section 3.1. Dr. J. C. Cutting was responsible for the current leakage program discussed in Section 3.2. The boundary layer diagnostic work given in Sections 4.1 and 4.2 was conducted by Dr. S. A. Self, Senior Research Associate. Dr. Robert Kessler assisted with much of the laboratory program and Mr. Frank Levy's assistance in the experimental work was invaluable.

## ABSTRACT

The research program described in this Final Report has included work on boundary layer studies, current distribution, and current leakage in magneto-hydrodynamic (MHD) generators, and boundary layer diagnostics. A computer program which has been used successfully to calculate conventional turbulent boundary layers has been modified by adding the MHD terms in the momentum and energy equations. This modified program has been coupled to a one-dimensional core-flow program to give boundary layer parameters in an MHD generator. Experiments were made in arc-heated argon with small additions of  $N_2$  and  $CO_2$  to delineate the effect of these components on electrode voltage drops. The effect was larger than could be predicted from ambipolar diffusion theory. Analysis and experiments made with electrodes of several sizes showed the important influence of boundary layer and electrode temperatures. Because the boundary layer temperature is coupled to the electrode temperature, small cold electrodes performed better than large cold electrodes in the Stanford MHD generator.

Current patterns in conducting wall generators were measured and showed good agreement with theoretical predictions for the anode. The surface-sheath voltage drop was responsible for less good agreement at the cathode. It was shown that a large fraction of the current entered the sidewalls of a conducting wall generator. Experiments also indicated that Faraday electrodes which included part of the sidewall gave a greater power output than conventional flat electrodes. Axial current leakage in the hall direction was calculated and measured in a simulated MHD generator using argon with up to 20%  $N_2$  diluent. Agreement between experiment and theory was satisfactory. For combustion gases with diffuse currents the theory predicts larger Hall voltages before breakdown than have been observed in practice. The Hall voltage limitation is believed associated with arcing phenomena.

A new method which uses Faraday splitting of laser modes is suggested for the measurement of electron concentration in the boundary layer. A laser doppler velocimeter and its applications to boundary layer velocity measurements in the Stanford generator is described.



## CONTENTS

Chapter	Page
1.0 Introduction	1
2.0 Boundary Layer Studies	2
2.1 Computer calculations of boundary layer parameters	2
2.2 Investigation of the effects of molecular gases on electrode voltage losses	8
2.3 Measurement of the effect of electrode size on the performance of an MHD generator	13
3.0 Current Distribution and Leakage Studies	14
3.1 Electrode current distribution	14
3.2 Axial current leakage in segmented MHD generators	15
4.0 MHD Generator Boundary Layer Diagnostics	16
4.1 Electron number density measurement	17
4.2 Velocity measurement by a laser doppler velocimeter	22
4.2.1 Introduction	22
4.2.2 Basic Design Considerations	23
4.2.3 Detailed Design Considerations	38
4.2.4 Component Specifications and System Characteristics	47
4.2.5 Alignment and Preliminary Testing	50
4.2.6 Summary and Conclusions	70
5.0 Summary	72
References	73

## ILLUSTRATIONS

<u>Figure No.</u>	<u>Title</u>	<u>Page</u>
1	Schematic of Boundary Layer Experiment . . . . .	4
2	Computed Axial Variation of Pressure and Velocity .	5
3	Boundary Layer Profiles at Approximate Channel Exit.	6
4	Normalized Boundary Layer Profiles at Approximate Channel Exit . . . . .	7
5	Cathode Voltage Drop with Argon Plus Additives . .	9
6	Effect of CO <sub>2</sub> on Cathode Voltage Drop . . . . .	11
7	Effect of CO <sub>2</sub> on Anode Voltage Drop. . . . .	12
8	Particle Scattering Geometry . . . . .	23
9	Oscilloscope Velocity Display . . . . .	26
10	Beam Focusing Diagram . . . . .	29
11	Optical Configuration . . . . .	30
12	Plan View of Port . . . . .	40
13	Vertical Section through Port . . . . .	41
14	Optical Layout . . . . .	45
15	Laser Mode Structure . . . . .	51
16	Fabry-Periot Drive Circuit . . . . .	52
17	Influence of Pinhole Size on Response . . . . .	59
18	Results from Cold Test with Water Atomiser . . . . .	61
19	Particle Mixing and Injection System . . . . .	66
20	Results from Hot Test with 5μ Alumina particles . .	68

## 1.0 INTRODUCTION

The High Temperature Gasdynamics Laboratory of Stanford University has been investigating losses originating near or in the boundary layer of an Magnetohydrodynamic (MHD) generator with a view to reducing these losses. The research program has been directed at experimental and analytical studies of the electrode boundary layer, of the current distribution and leakage as influenced by the boundary layers, and at diagnostic techniques which appear capable of the necessary spatial resolution to be useful in the boundary layer.

Certain parts of the effort have been completed and have been reported in Air Force Aero Propulsion Laboratory reports. Other parts of smaller scope have been reported in the technical literature. Work which was underway near the conclusion of the contract has not been previously reported and is given in more detail in this final report.

The following publications have resulted from the program conducted under contract F33615-72-C-1171:

"Effects of Electrode Size on the Performance of a Combustion-Driven MHD Generator," E. S. Rubin, SU-IPR Report #335, August 1969.

"A Computer Program for the Calculation of the Electron Transport Coefficients," M. Mitchner, SU-IPR Report #280, August 1969.

"Axial Current Leakage in Segmented MHD Generators," J. C. Cutting, SU-IPR Report #406, January 1971.

"Measurement of Current Distributions and the Effect of Electrode Configuration on MHD Generator Performance," R. H. Eustis and R. Kessler, Fifth Intl. Conf. on MHD Electrical Power Generation, I, April 1971.

"Axial Current Leakage in Segmented MHD Generators," J. C. Cutting and R. H. Eustis, Fifth Intl. Conf. on MHD Electrical Power Generation, I, April 1971.

"Effects of Electrode Size on the Performance of a Combustion-Driven MHD Generator," E. S. Rubin and R. H. Eustis, AIAA Journal, Vol. 9, No. 6, June 1971.

"Axial Current Leakage Between Electrodes in MHD Generators," J. C. Cutting, R. H. Eustis, Eleventh Symposium on Engineering Aspects of Magnetohydrodynamics, 1970.

"Electrode Size Effects in Combustion-Driven MHD Generators," E. S. Rubin, R. H. Eustis, Eleventh Symposium on Engineering Aspects of Magnetohydrodynamics, 1970

"Effects of Electrode Size on MHD Generator Performance," E. S. Rubin, R. H. Eustis Tenth Symposium on Engineering Aspects of Magnetohydrodynamics, 1969.

"Current Distribution in Conducting Wall MHD Generators," R. H. Eustis, R. M. Cima, and K. E. Berry, Eleventh Symposium on Engineering Aspects of Magnetohydrodynamics, 1970.

The present report which constitutes the final report for contract F33615-69-C-1171 is divided into three major sections. The first deals with the boundary layer analysis and with experiments related to effects influencing the near-electrode region. The second section is concerned with the calculation and measurement of current distribution in a conducting wall generator and with current leakage in the Hall direction. The last section deals with diagnostic techniques. A brief summary concludes the report.

## 2.0 BOUNDARY LAYER STUDIES

In this section a description of the analysis of the turbulent MHD boundary layer and some computer results are given, the measurements relating to the effect on electrode voltage drops due to molecular species are described, and the results of tests with different electrode sizes are presented.

### 2.1 Computer calculations of boundary layer parameters

In order to take advantage of the large amount of work which has been done in developing computer programs to calculate conventional turbulent boundary layers, the excellent program of Patankar and Spalding [1]\*as modified extensively by Kays and coworkers [2] has been used as a basis for our calculations. The basic equations have been modified to include the MHD terms as follows:

x - momentum equation

$$\rho \left( u \frac{\partial u}{\partial x} + v \frac{\partial u}{\partial y} \right) = j_y B \frac{\partial p}{\partial x} + \frac{\partial}{\partial x} \left( \mu \frac{\partial u}{\partial y} \right)$$

y - momentum equation

$$j_x B + \frac{\partial p}{\partial y} = 0$$

---

\*Numbers in square brackets refer to the References.

energy equation

$$\rho u \frac{\partial h_o}{\partial x} + \rho v \frac{\partial h_o}{\partial y} = \frac{\partial}{\partial y} (u \tau_{xy}) + \vec{E} \cdot \vec{j} + \frac{\partial q_y}{\partial y}$$

where

$$\tau_{xy} = \mu_{eff} \frac{\partial u}{\partial y}$$

$$q_y = k_{eff} \frac{\partial T}{\partial y}$$

For computational convenience the above equations have been rewritten in terms of the variables

$$\psi_x = -\rho v \quad \text{and} \quad \psi_y = \rho u$$

as suggested by von Mises [1] in order to automatically satisfy the continuity equation. The Kays - Patankar - Spalding computer program has been altered to account for the extra terms due to the MHD effects and runs have been made as described later.

It is necessary to give the computer program a pressure distribution which is derived from a one-dimensional analysis of the core flow. This analysis uses the boundary layer displacement thickness as a correction for the core flow area distribution so interaction between the core flow and boundary layer programs is required. The core flow analysis makes use of the standard momentum, energy and continuity equations

$$\rho u \frac{du}{dx} + \frac{dp}{dx} = (\vec{j} \times \vec{B})_x$$

$$\rho u \frac{dh_o}{dx} = \vec{E} \cdot \vec{j} + q_{rad}'''$$

$$\rho A_{eff} V = \text{constant}$$

where  $A_{eff}$  is the flow area corrected for the boundary layer and the radiation term includes band radiation from  $CO_2$  and  $H_2O$  and line radiation from the potassium seed.

An experimental program has been planned to measure the boundary layer velocity and temperature profiles in an MHD generator and the proposed operating conditions are shown in Figure 1. An illustration of the application of the computer program, the calculated profiles and other parameters for

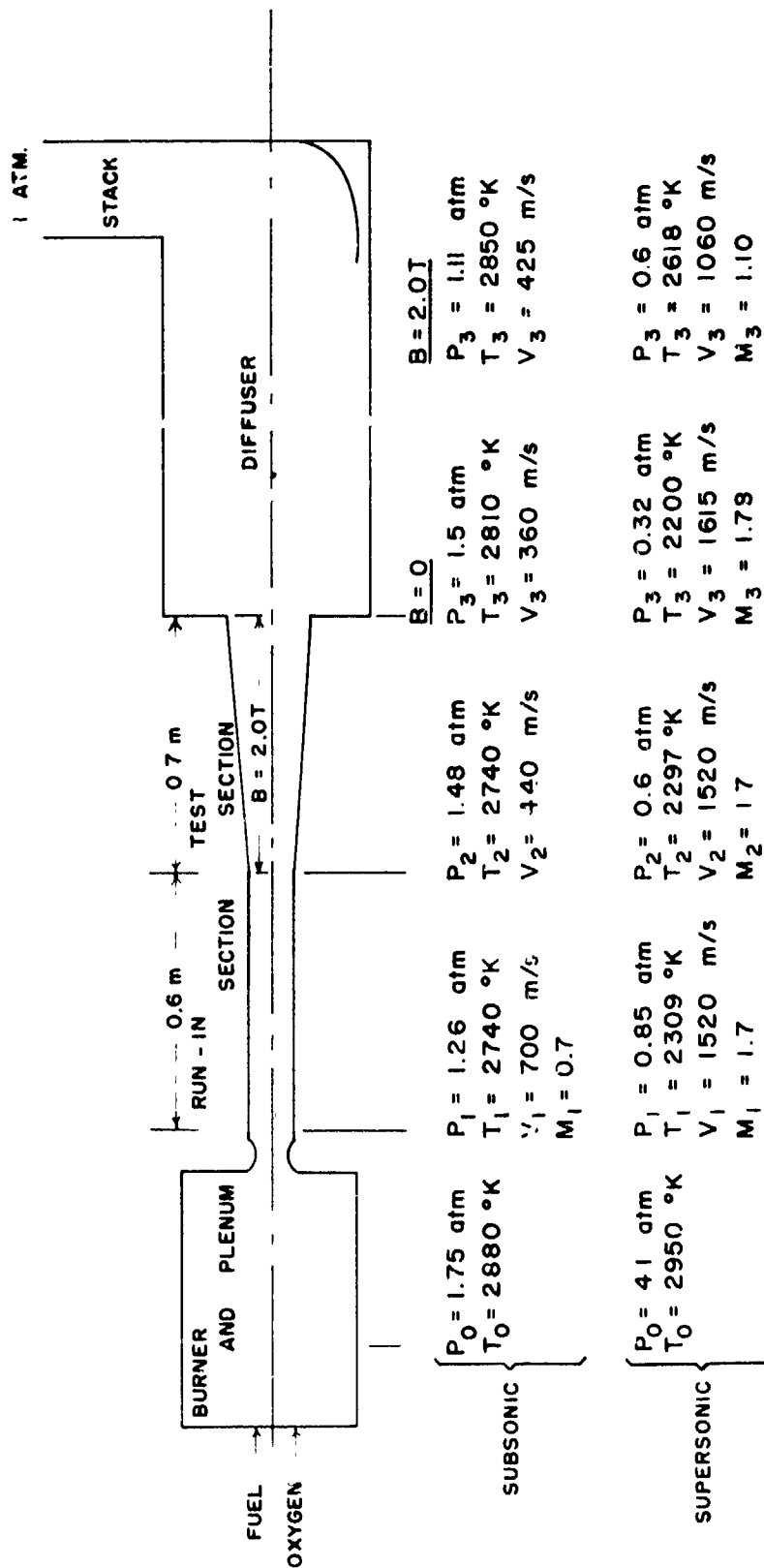


Figure 1 Schematic of Boundary Layer Experiment

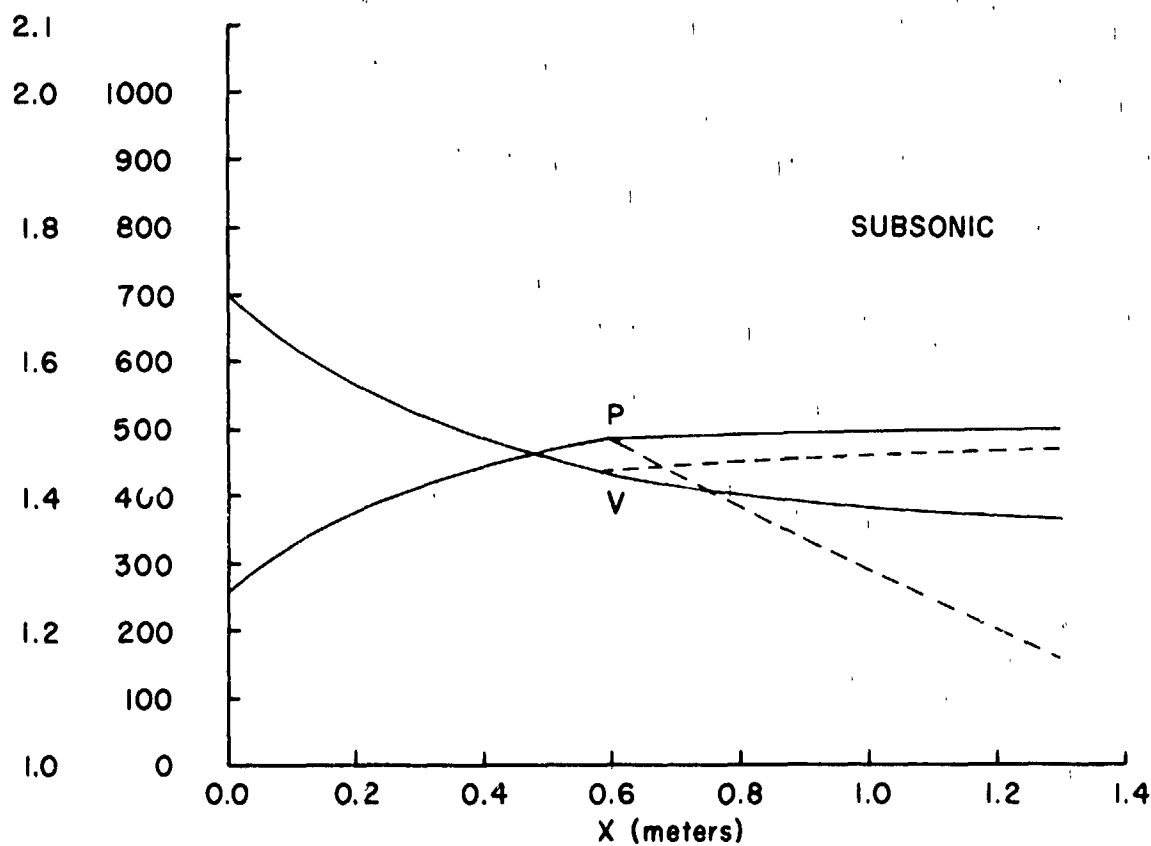
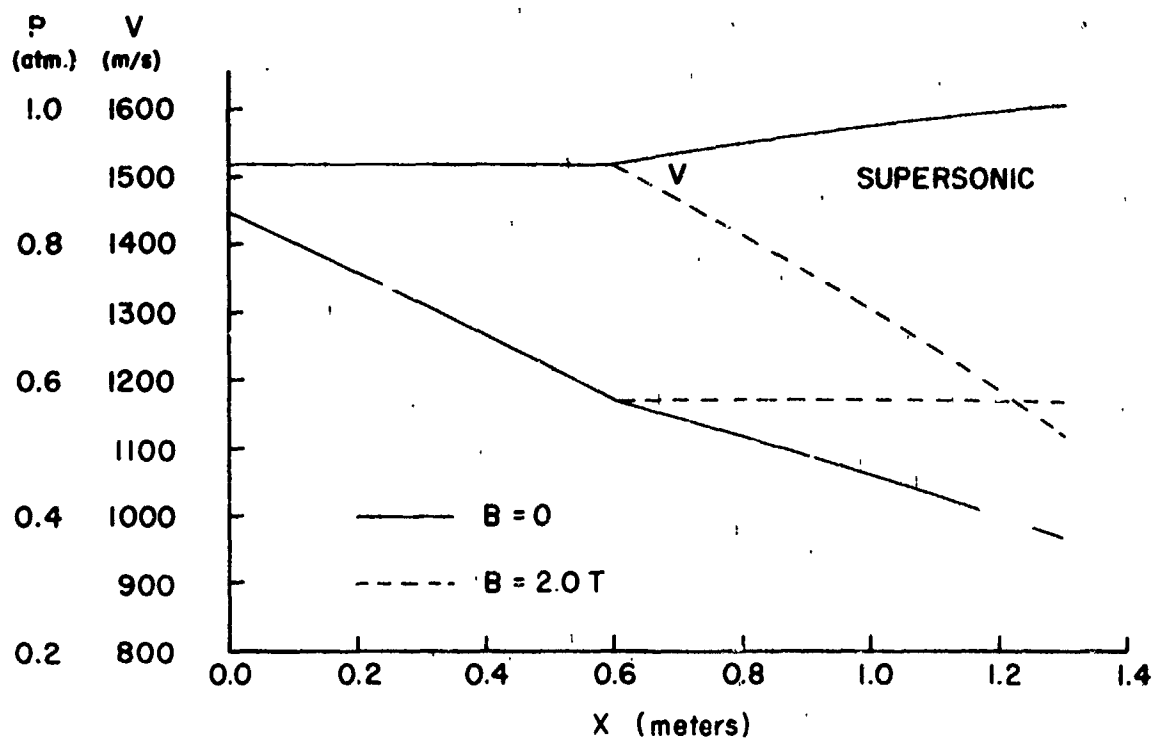


Figure 2 Computed Axial Variation of Pressure and Velocity

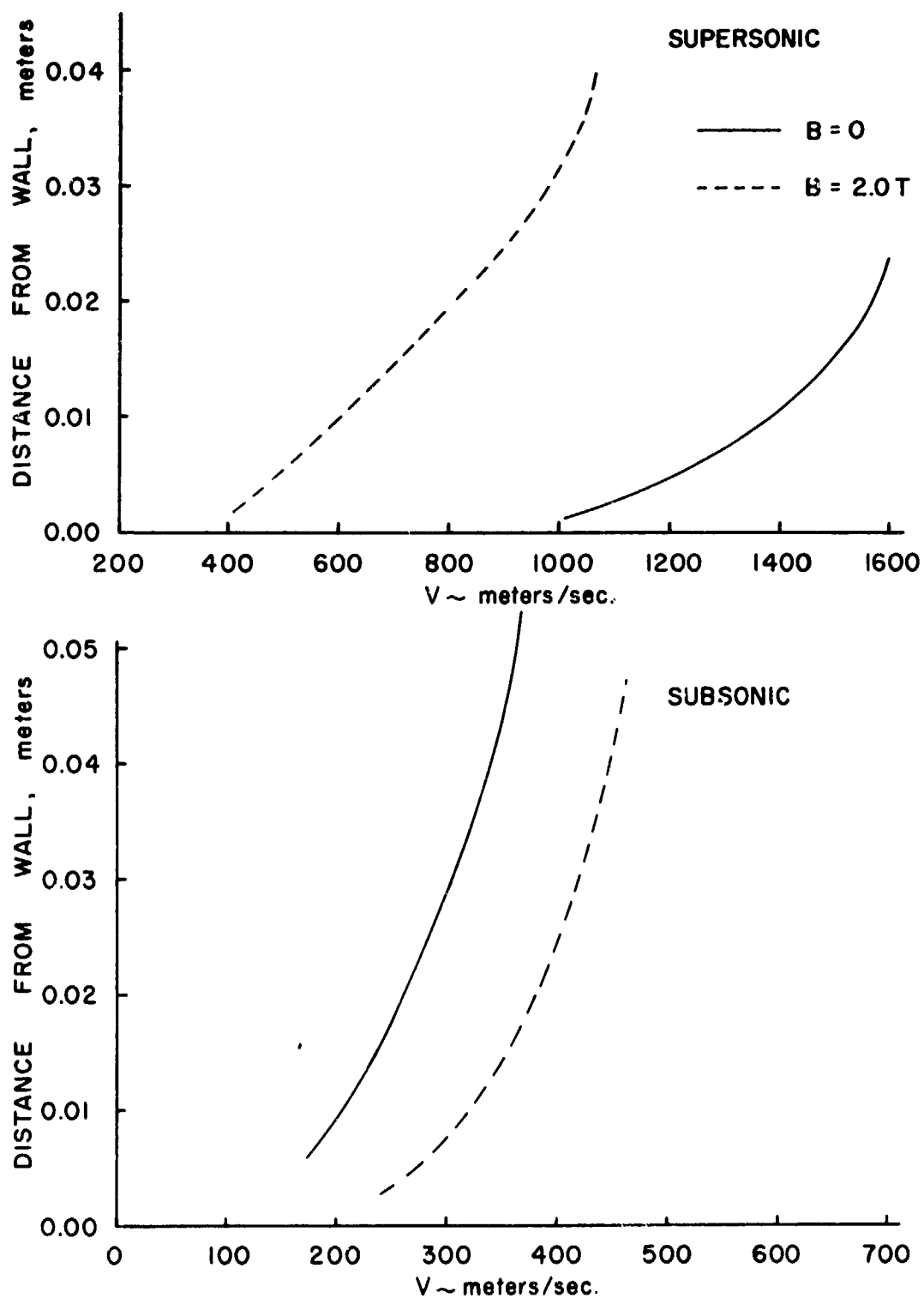


Figure 3 Boundary Layer Profiles at Approximate Channel Exit



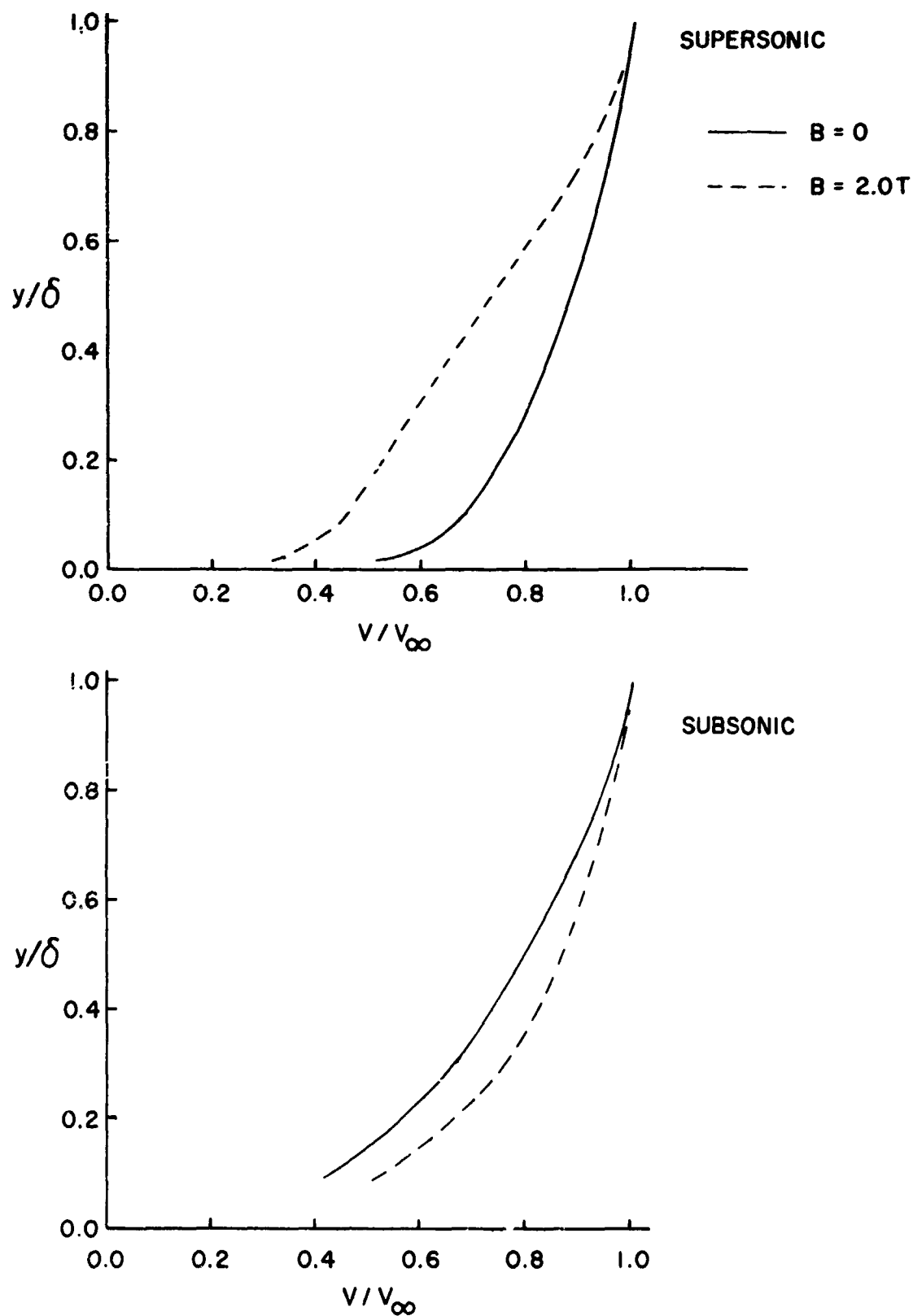


Figure 4 Normalized Boundary Layer Profiles at Approximate Channel Exit

the proposed experiment are shown in Figures 2 to 4. It is seen that two major test conditions are planned -- one subsonic and the other supersonic. The apparatus consists of the burner and plenum followed by a run-in section 0.6 meter long and the test section 0.7 meter long which is inserted in the magnet. The run-in section is to thicken the boundary layer to facilitate measurements and to more closely simulate larger scale generators.

The variation of the core velocity and the pressure with axial distance measured from the nozzle is shown in Figure 2. The dotted lines which show the case for  $B = 2$  tesla indicate opposite effects for subsonic and supersonic flow as is expected. Velocity profiles near the end of the test section are shown in Figure 3 and are plotted in a normalized fashion in Figure 4. It is clear that the profile is modified in shape as well as in the magnitude of velocities by the MHD effect.

Measurements of the velocity near the outer edge of the boundary layer were conducted under contract F33615-69-C-1171 as discussed in section 4.2 of this report. Further measurements are being conducted under contract F33615-72-C1088.

## 2.2 Investigation of the effects of molecular gases on electrode voltage losses.

A series of experiments designed to obtain an understanding of the nature of electrode voltage drops in combustion-gas MHD generation were performed. The objective of these experiments and associated theoretical work was to be able to predict the magnitude of this important loss mechanism for proposed MHD generator designs.

A series of three experiments have shown that the addition of small amounts of carbon dioxide into an argon-potassium seeded plasma has substantial effect on electrode voltage drop behavior. With the addition of 5%  $\text{CO}_2$ , cathode voltage drops comparable to those exhibited in combustion-gas experiments, have been measured. (See Figure 5 )

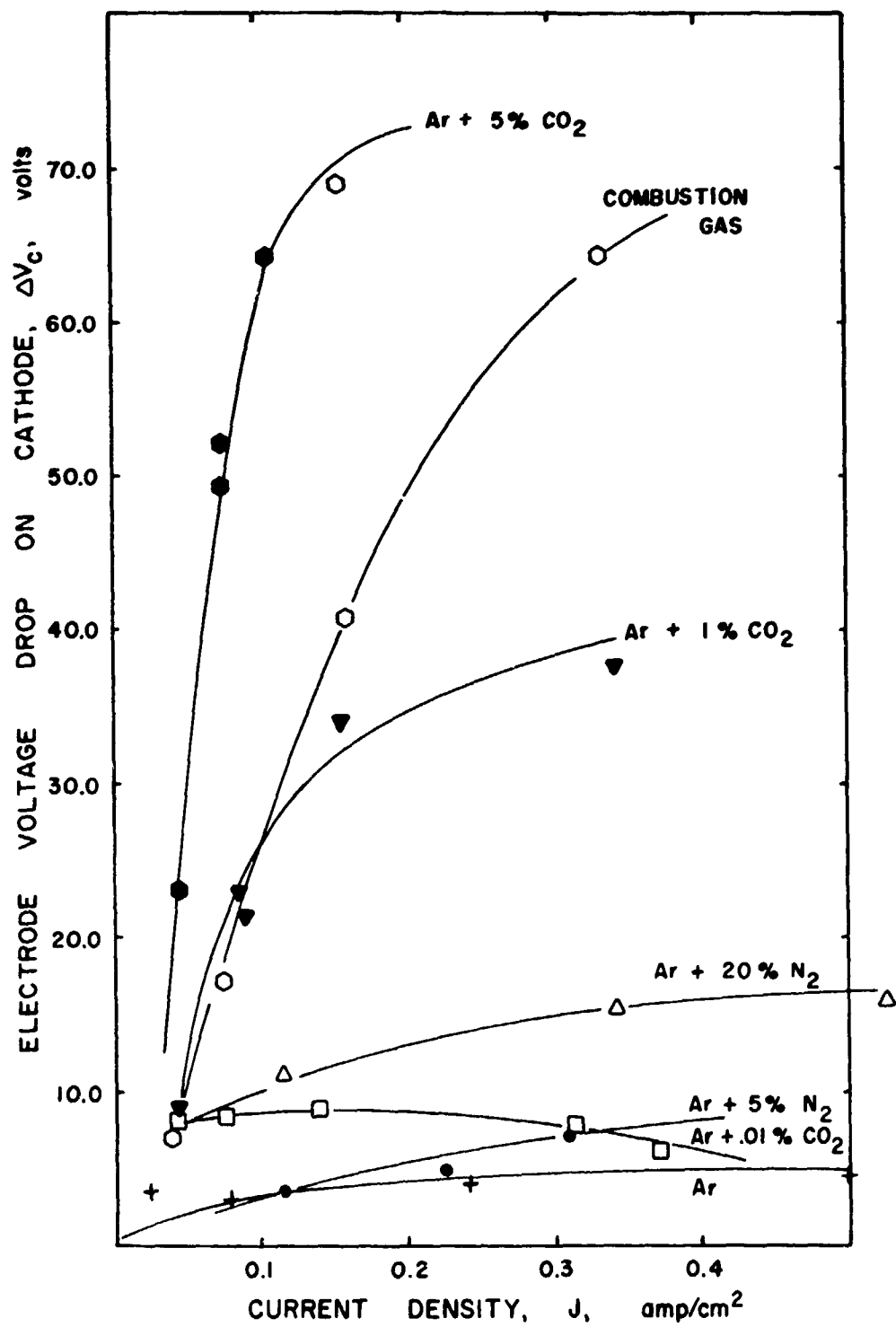


Figure 5. Cathode Voltage Drop with Argon Plus Additives

The experimental apparatus consisted of an argon arc jet, a plenum chamber where controlled amounts of potassium seed and molecular gases were introduced and a quartz test section in which a discharge was imposed across multiple pairs of segmented electrodes. Voltage drops were measured by means of an array of probes located between the discharge electrodes. The gas temperature was in the range 1900°K and the electrode temperature was approximately 1400°K. Potassium seeding was 0.2% (mass fraction) and CO<sub>2</sub> addition was varied from 0% to 5%. With externally applied voltages, current densities up to 0.5 amps/cm<sup>2</sup> were measured.

Figure 5 shows the relative magnitudes of electrode voltage drops in various experimental situations. The combustion gas data is taken from Kessler [3] and the nitrogen-argon data was provided by Cutting [4]. Figures 6 and 7 show the results of cathode and anode voltage drops respectively versus current density for the first two experiments. Similar behavior was obtained in the third experiment, but different gas conditions did not allow comparison on these figures.

From these data the following observations may be made:

- (1) For specified gas conditions, i.e., for specified electrode and gas temperatures and seed fraction, increasing addition of CO<sub>2</sub> resulted in higher voltage drops.
- (2) Electrode voltage drops were linear with current density for small current densities.
- (3) Relatively small additions of CO<sub>2</sub> have substantial effects on electrode behavior, especially at the cathode. (e.g., .01% CO<sub>2</sub> addition essentially doubles the cathode voltage drop.)
- (4) Cathode voltage drops are several times larger than the corresponding anode drops.

A theoretical interpretation of these results has been attempted on the basis of an ambipolar - diffusion model which accounts for the boundary-layer temperature profile. This model has been moderately successful in predicting

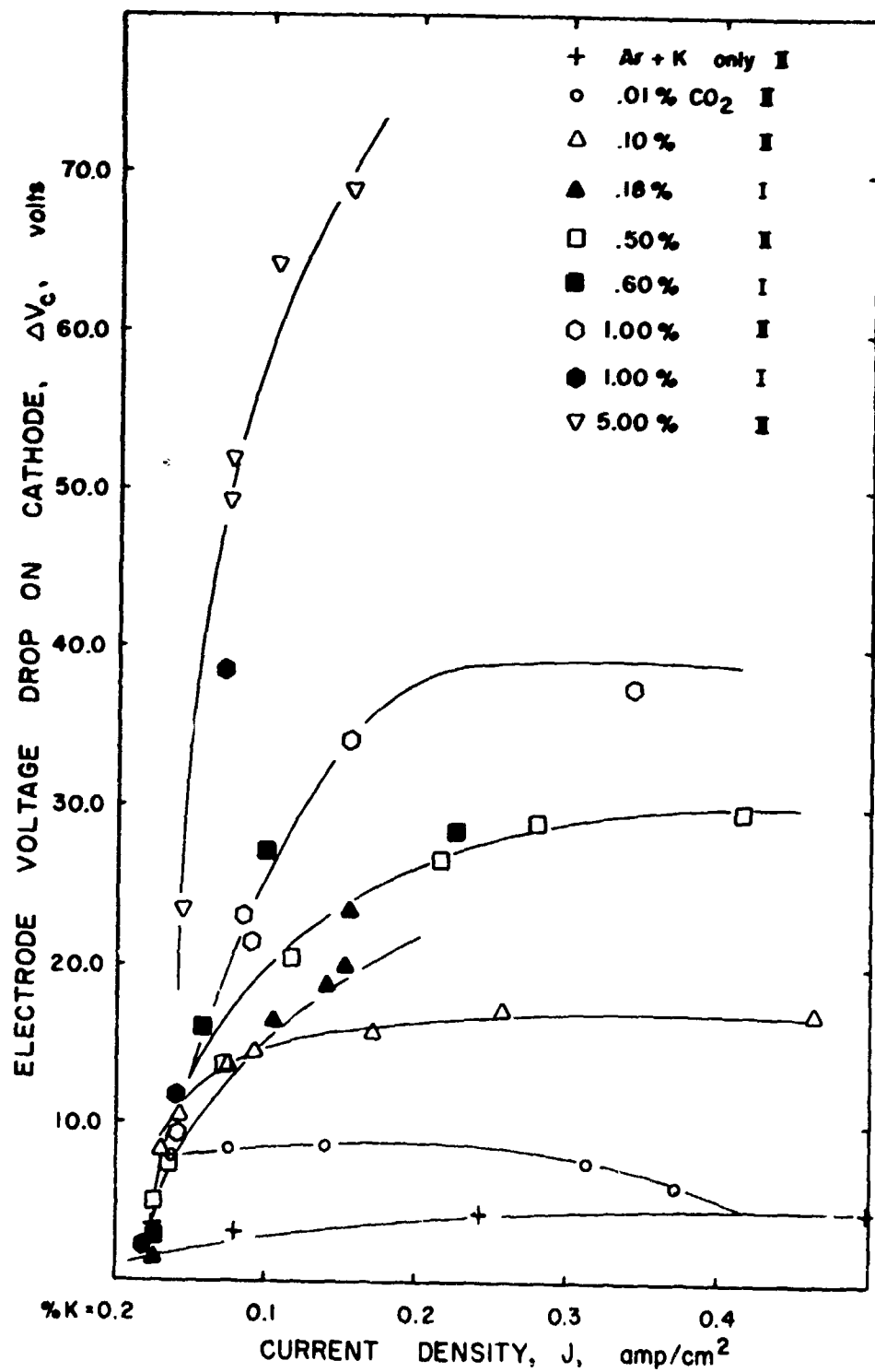


Figure 6. Effect of CO<sub>2</sub> on Cathode Voltage Drop

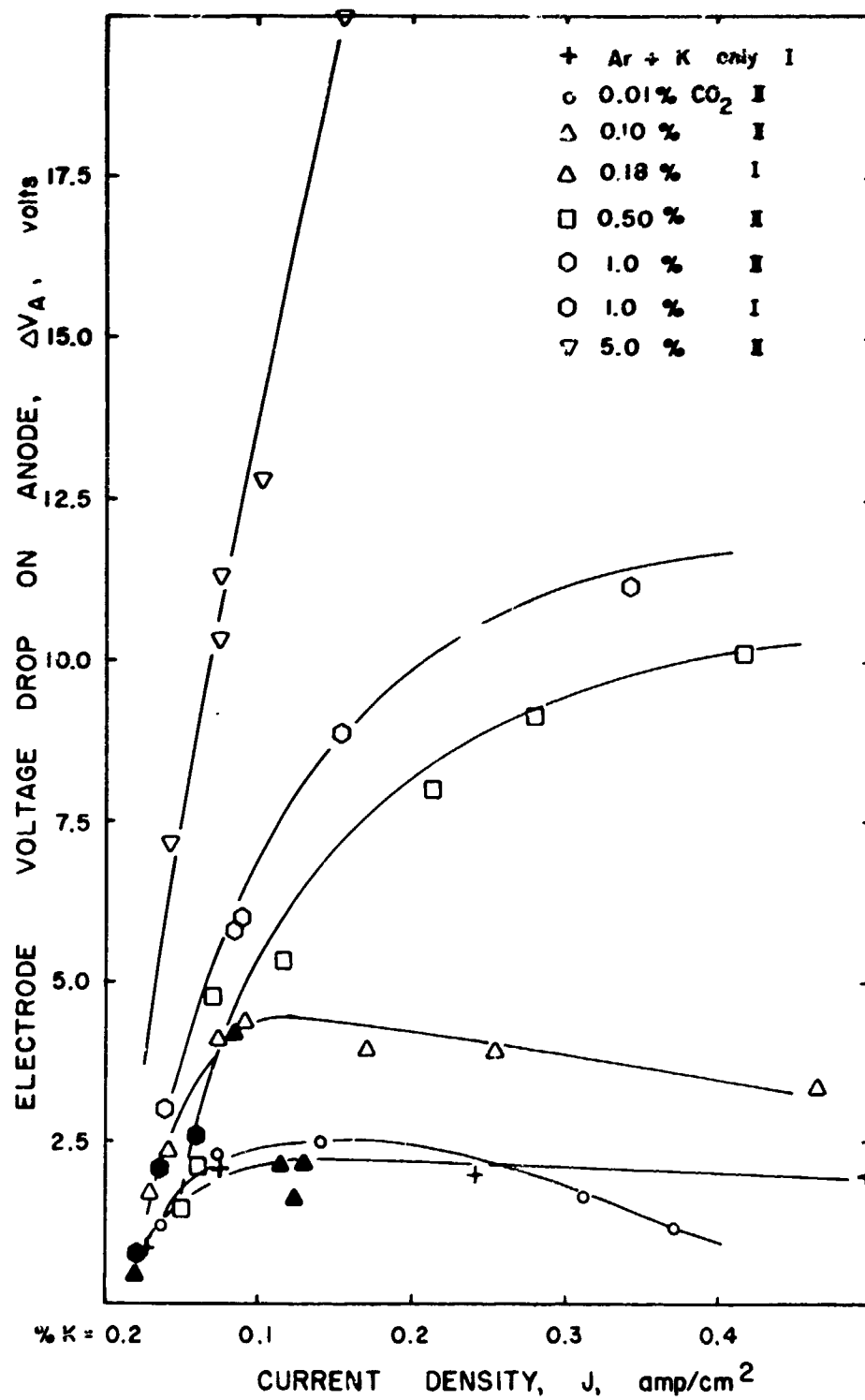


Figure 7. Effect of CO<sub>2</sub> on Anode Voltage Drop

the observed behavior, but it appears that additional features must be incorporated to obtain an accurate description.

This work will be completely described in a forthcoming Stanford report which will be sent to the Aero Propulsion Laboratory.

### 2.3 Measurement of the effect of electrode size on the performance of an MHD generator

Experiments were conducted to investigate the effects of electrode size on the performance of a combustion-driven MHD generator. Electrode sizes with length-to-pitch ratios of 0.23, 0.50, and 0.79 were tested in a generator section simulated by three molybdenum electrode pairs located at the downstream end of an MHD channel. Voltage probe data were obtained for electrode surface temperatures between 500°K and 1600°K, with gas conductivity in the electrode boundary layer regions established independently by either a hot (2200°K MgO brick) or cold (750°K water-cooled plate) upstream wall. At a given load current, larger electrodes were found to have lower voltage losses for similar conditions of surface and gas boundary-layer temperature. For dissimilar boundary layers, reflecting coupling between electrode and boundary-layer temperatures in a cold-electrode generator, total voltage losses for a large electrode pair were equal to or greater than those of a small electrode pair at the same surface temperature. Experimental boundary-layer resistances at anodes were in good agreement with analytical predictions based on both an approximate and a more exact gas-dynamic model, for electrode temperatures above about 800°K. At lower temperatures anodes were believed to be influenced by solidification of seed compounds on the electrode surfaces, resulting in higher losses. For cathodes, the boundary-layer resistance was gasdynamic for the case of a hot upstream wall, for electrode current densities below that of saturated thermionic emission at the electrode temperature. In all other cases, the presence of cathode surface-sheath effects was indicated.

This work has been reported in detail in Air Force Technical Report No. AFAPL-TR-69-72 and in AIAA Journal, Vol. 9, No. 6, June 1971, pp. 1162-29.

### 3.0 CURRENT DISTRIBUTION AND LEAKAGE STUDIES

Two major efforts of contract F33615-69-C-1171 were devoted to the calculation and measurement of electrode current distribution in a conducting wall generator and to the calculation and measurement of Hall current leakage in a simulated MHD generator. Both of these programs have been reported in detail in the literature and are summarized below.

#### 3.1 Electrode current distribution

An experimental program was conducted to investigate the performance of a combustion-driven MHD generator with conducting sidewalls and with various electrode configurations. The current distribution to the electrodes and conducting sidewalls of a Hall generator was measured. The Hall generator was operated with both conducting and with insulating sidewalls; no significant performance differences were found. Significant current was found to flow to the sidewall segments of the conducting-wall Hall generator, especially to those segments immediately adjacent to the normal electrodes. An experiment was made with a Faraday generator in which the electrodes included the immediately adjacent sidewall segments. This generator produced about 25% more power than a conventional Faraday generator with flat electrodes.

This type of electrode in which part of the current enters (or leaves) the electrode parallel to the magnetic field may be of special interest for high magnetic field generators. Current concentrations should be reduced over those on flat electrodes and higher Hall voltages may therefore be possible.

A computation procedure was developed for calculating the current distribution in the plane perpendicular to the velocity vector. Appropriate turbulent velocity and temperature profiles were assumed and the results agreed well with the measured anode current distribution. The agreement of measured and predicted current distributions at the cathode was less satisfactory, probably because of



the cathode surface-sheath voltage drops which were not accounted for in the model.

This work has been reported in detail in the following publications:

Eustis, Cima, Berry, "Current Distribution in Conducting Wall Generators," Eleventh Symposium on Engineering Aspects of Magnetohydrodynamics, 1970, and Eustis, Kessler, "Measurement of Current Distributions and the Effect of Electrode Configuration on MHD Generator Performance," Fifth Intl. Conf. on MHD Electrical Power Generation, I, April 1971.

### 3.2 Axial current leakage in segmented MHD generators

Experiments were performed in a simulated linear, segmented MHD generator to investigate the phenomenon of axial current leakage between electrodes. An argon-potassium plasma was used with the addition of up to 20 percent nitrogen to suppress non-equilibrium effects. Electric and magnetic fields were applied to provide a maximum average transverse current density of 2 amperes per sq cm and a maximum Hall parameter of 6.

The generator was composed of six tungsten electrode pairs inserted into a rectangular quartz channel. The measuring or "test" electrode was electrically guarded and relaxation effects minimized by three upstream electrode pairs and two pairs downstream. The anode and cathode of this "test" electrode were divided into three segments each and the current direction and magnitude measured at each segment.

Axial current leakage between adjacent electrodes was measured and found to be a function of increasing transverse current density. The "critical" transverse current density necessary to cause leakage decreased with increased Hall parameter, decreased plasma temperature and decreased percentage of nitrogen additive. Leakage currents in excess of 50% of transverse currents were measured with no indication of breakdown or arcing between adjacent electrodes.

Hall voltages were observed to have an asymptotic limit with increasing transverse current density. The value of this limit was a function of nitrogen percentage and Hall parameter.

A computer program for calculation of electrical current distributions in a segmented MHD device was written to interpret and predict the experimental data. The program consisted of a coupled solution of the current stream function equations and the electron energy and continuity equations. It was found that the Hall voltage data and the measured cathode current phenomena were well predicted by the theory. Prediction of current leakage at the anode wall did not compare as well with the measured results. The calculations indicated that the increase in electrical conductivity along the electrode walls was responsible for axial current leakage.

For combustion gases where the electrical conductivity is nearly independent of current density (for modest densities) the calculations showed that current leakage would not occur for Hall fields several times those achieved in practice. It is believed that the Hall breakdown which has occurred in generators is associated with arcing rather than a limitation which would occur for diffuse currents.

This work has been reported completely in Air Force Technical Report No. AFAPL-TR-71-23, January, 1971, by John C. Cutting and in the paper by Cutting and Eustis, "Axial Current Leakage Between Electrodes in MHD Generators," Eleventh Symposium on Engineering Aspects of Magnetohydrodynamics, 1970.

#### 4.0 MHD GENERATOR BOUNDARY LAYER DIAGNOSTICS

In an MHD generator boundary layer three of the important quantities which need experimental determination are gas temperature, gas velocity, and electron number density. The measurement of gas temperature was described in a report for contract AF F33615-67-C-1127, Technical Report No. AFAPL-TR-68-141. In the sections below a suggested new method of measuring electron number density

with good spatial resolution is described and the development and testing of a laser doppler velocimeter is given. This latter topic was a major diagnostic effort of contract AF F33615-69-C-1171.

#### 4.1 Electron number density measurement

A new method is described for measuring electron concentration in a magnetoplasma by observing the beat frequency due to Faraday splitting of a laser mode when the plasma is situated in the laser cavity with the magnetic field along the laser axis. It appears to offer a number of advantages over conventional laser interferometric methods with regard to sensitivity and spatial resolution.

In conventional interferometric methods for determining electron number density  $n$  at microwave or optical frequencies [5], the minimum density (or density change) that can be measured is set by the requirement that the density line integral  $\int_0^{\ell} n dx = \bar{n}\ell$  should give a detectable phase shift. For an unmagnetized plasma the refractive index is  $\mu = (1 - f_p^2/f^2)^{1/2} = (1 - n/n_c)^{1/2}$  where  $f_p = 8.97 \times 10^3 n^{1/2}$  is the plasma frequency and  $n_c = 1.24 \times 10^{-8} f^2$  is the cut-off density for the source frequency  $f = c/\lambda$  (cgs units). For  $f \gg f_p$  the phase shift  $\Delta\phi$  is given by

$$\frac{\Delta\phi}{2\pi} = \frac{(1-\mu)\ell}{\lambda} = \frac{1}{2} \frac{\bar{n}}{n_c} \frac{\ell}{\lambda} = \frac{\bar{f}_p^2 \ell \lambda}{2c^2} \approx 4.5 \times 10^{-14} \bar{n} \ell \lambda, \quad (1)$$

and the minimum detectable density line integral, or resolution is

$$(\bar{n})_{\min} \approx \frac{2.2 \times 10^{14}}{\lambda} \frac{\Delta\phi}{2\pi} \quad (2)$$

where  $(\Delta\phi/2\pi)_{\min}$  is the minimum detectable fractional fringe shift. In practice this is about (1/10) fringe, though it may be improved to  $\sim(1/100)$  fringe by various sophisticated techniques.

For laboratory plasmas of dimensions typically  $\ell = 1 - 100$  cm, it transpires that microwaves (up to the maximum practical frequency  $\sim 10^{11}$  Hz) are satisfactory for densities  $n \lesssim 10^{13} \text{ cm}^{-3}$ , while visible or near infrared lasers are useful for densities  $n \gtrsim 10^{16} \text{ cm}^{-3}$ . For the important intermediate range of densities

$10^{13} \leq n \leq 10^{16}$ , of particular interest for fusion and MHD studies, far infrared lasers (e.g. HCN at 337  $\mu\text{m}$ ) have recently been employed [6-8].

While resolution in density is the primary criterion in the choice of frequency, spatial resolution is also important. The narrow, low-divergence beams of visible and near infrared lasers give good spatial resolution but are insufficiently sensitive except for very high densities. It is clear that if the sensitivity could be markedly increased, then visible or near infrared lasers could be used in the intermediate range of densities, with a great gain in spatial resolution. Moreover, visible and near infrared lasers, together with the associated optical techniques, are more highly developed and readily available than their far infrared counterparts.

A very great increase in sensitivity may be achieved [5,9] by incorporating the plasma into the laser cavity so that it controls the frequency. For a mirror spacing  $L$ , the frequency shift  $\Delta f$  produced by the plasma is given by

$$\frac{\Delta f}{f} = \left( \frac{L}{2L} \right) \left( \frac{f_p^2}{f^2} \right) = \left( \frac{L}{2L} \right) \left( \frac{\bar{n}}{n_c} \right) \quad (3)$$

while the resolution is

$$(\bar{n}L)_{\min} \approx 3.7 \times 10^2 \left( \frac{2L}{\lambda} \right) \Delta f_{\min} \quad (4)$$

where  $q = (2L/\lambda)$  is the axial mode number. The minimum frequency shift  $\Delta f_{\min}$  that can be detected is determined by the frequency stability of the laser and of the frequency reference, which may be either a cavity resonator (Fabry-Perot etalon) or another identical laser. In practice far greater sensitivity is obtained by heterodyning against a second laser.

By using two He-Ne lasers, Johnson [5,9] has been able to measure frequency shifts on repetitive signals (pulsed plasma) as low as 1 kHz, corresponding to a density of  $2 \times 10^{10} \text{ cm}^{-3}$  in a plasma 30 cm long. To achieve this

resolution interferometrically would require detection of a fringe shift of  $10^{-6}$ . However, this great sensitivity is achieved only at the expense of severe difficulties associated with thermal and mechanical instability of the lasers. Furthermore, because under these conditions the free electron contribution to the refractive index is less than  $10^{-10}$ , it may be completely masked by the contribution due to excited atoms and ions. Johnson overcame this problem by simultaneous measurements at  $\lambda = 0.633$  and  $1.152 \mu\text{m}$ , so that by subtraction the frequency-dependent part of the refractive index due to free electrons was obtained.

In the new method proposed here, we take advantage of the increased sensitivity resulting from placing the plasma in the laser cavity but, by using Faraday splitting, we avoid the complication of a second laser and the associated stability problems.

For propagation along the direction of a static magnetic field  $B$ , the plasma refractive index is

$$\mu_{\pm} = \left[ 1 - \frac{f_p^2}{f(f \pm f_c)} \right]^{1/2} \approx 1 - \frac{1}{2} \frac{f_p^2}{f^2} \left[ 1 - (\pm) \frac{f_c}{f} \right] \quad (f \gg f_p, f_c) \quad (5)$$

where  $f_c$  is the electron cyclotron frequency, and the signs correspond to the left (+) and right (-) circularly polarized waves defined relative to the direction of  $B$ .

In the absence of a gyrotropic medium a given laser mode  $\text{TEM}_{00q}$  is linearly polarized and may be regarded as the superposition of right and left circularly polarized modes. The inclusion of an axially magnetized plasma in the laser cavity is just  $\Delta f$  given by Eq. 3, while the differential shift  $\delta f$  is given by

$$\frac{\delta f}{f} = \left( \frac{\ell}{L} \right) \left( \frac{f_p^2}{f^2} \right) \left( \frac{f_c}{f} \right). \quad (6)$$

Thus the differential shift is smaller than the average shift by a factor  $(2f_c/f)$ , while the resolution is

$$(\bar{n}l)_{\min} \approx 3.7 \times 10^2 \left( \frac{L}{\lambda} \right) \left( \frac{f_c}{f} \right) \delta f_{\min} . \quad (7)$$

Combining the two component modes it is seen that they correspond to a composite plane polarized mode whose plane of polarization rotates at a frequency  $(\delta f/2)$ . Hence, by passing the laser output through a linear polarizer, the frequency difference may be detected directly as an amplitude modulation at frequency  $\delta f$ .

Thermal and mechanical fluctuations will affect the component modes equally, so that the problems of frequency stability associated with the beating of two lasers are avoided. Moreover, the component modes will experience the same tuning due to bound electrons, so that perturbations due to atoms and ions cancel and the method should work well in weakly ionized plasmas. Another feature is that, unlike other methods, there is in principle no need to switch off the plasma to establish a reference phase or frequency, so that the method is appropriate for steady-state plasmas, for example MHD flows, which cannot easily be switched on and off. On the other hand the low beat frequency would preclude fast time resolution with pulsed plasmas. However, this may be overcome by using a suitable frequency off-set or bias as described below.

It is clear that to allow the linearly polarized mode to rotate, the laser must have rotational symmetry. Thus Brewster windows are precluded; all windows must be normal to the axis and should be anti-reflection coated. It also appears necessary to ensure operation in a single axial mode. While different axial modes will give the same splitting  $\delta f$ , so that the composite modes rotate at the same frequency, their planes of polarizations may be different and give rise to detected signals at multiples of  $\delta f$ .

It is anticipated that the minimum measurable frequency splitting  $\delta f_{\min}$  will be set by the tendency for closely spaced modes to lock together as a result of

stray coupling. The situation is similar to that in ring lasers [10], where scattering at the mirrors causes modes propagating in opposite directions around the ring to lock for rotations giving frequency shifts less than 100-1000 Hz. In the present case scattering at imperfections of the mirrors or windows may be expected to couple the component modes and lock the composite mode's plane of polarization onto the imperfections. Judging by ring laser experience this may be estimated to occur for splittings less than  $\sim 1$  kHz.

Mode locking may be prevented by producing a frequency bias, either by introducing an additional splitting with a Faraday rotator, or by Zeeman splitting of the laser modes [11] on application of a magnetic field. By biasing to a suitably high frequency and using a fast FM discriminator it appears that temporal resolution of density changes may be obtained for pulsed plasmas.

The feasibility of the proposed method depends, on the one hand, on the configuration and parameters  $f_p$ ,  $f_c$  of the plasma, and, on the other, on the availability of suitable lasers. Since the optical axis must lie along the magnetic field the method is suited for systems with axial symmetry such as mirror machines and for MHD flows. For example, in the combustion MHD facility at Stanford the duct width  $\ell \approx 10$  cm,  $B \approx 25$  kG and  $n_p \approx 10^{14}$  cm $^{-3}$ . Considering a He-Ne laser of mirror spacing  $L = 100$  cm, the frequency shifts  $\delta f$  calculated from Eq. 6 for the three commonly used Ne transitions are tabulated below.

$\lambda$ ( $\mu\text{m}$ )	$\delta f$ (kHz)
0.633	0.25
1.152	0.82
3.39	7.1

For these conditions the 0.633  $\mu\text{m}$  line gives a rather small shift and in any case might give difficulties because of its low gain in view of irreducible reflection losses at the windows. However, either the 1.152  $\mu\text{m}$  line or the high gain 3.39  $\mu\text{m}$  line appear to be convenient.

Finally it may be noted that for a plasma magnetized perpendicular to the laser axis one should get splitting into orthogonal linearly polarized modes corresponding to the ordinary and extraordinary plasma waves. However, in that case, the splitting is smaller again by a factor  $(f_c/f)$ .

## 4.2 Velocity measurement by a laser doppler velocimeter

### 4.2.1 Introduction

Measurement of the doppler shift of focused laser light offers a powerful non-perturbing technique for probing various types of fluid flows. Recently it has been used in a variety of flows including low-velocity liquid flows, hypersonic wind tunnels, rocket exhausts, and also in high temperature highly-ionized plasmas for thermonuclear fusion research. In principle it can yield information with high spatial resolution, on the average velocity and the turbulent velocity spectrum of the scattering centers. In the case of neutral or weakly-ionized gas flows, the effective scattering centers are macroscopic particles in the size range 1-10 micron which are either naturally present in the flow or deliberately added to facilitate the measurement.

For MHD flows, great interest attaches to the structure of the gas-dynamic boundary layer at the electrodes, and its modification by MHD action due to collisional coupling between the neutral gas and the plasma. The study of this boundary layer presents a considerably more challenging problem than appears to have been met hitherto using laser doppler techniques in other types of flows. The requirement on spatial resolution is particularly stringent. For typical conditions in the Stanford combustion M.H.D. channel, the boundary layer thickness is  $y_0 \sim 1$  cm, while, on the assumption of a seventh power velocity profile  $(u/u_0) = (y/y_0)^{1/7}$ , the position where the velocity  $u$  is half the free-stream value  $u_0$ , is only  $y \sim 0.1$  mm ( $\approx 100 \mu$ ) from the surface. Thus, to obtain useful data on the boundary layer, the spatial resolution should be comparable to or



better than this, and the instrument must be capable of measuring the flow velocity to within this distance of an incandescent electrode. Other problems involve obtaining optical access to the measurement point without disturbing the flow or exposing the window to damage from the hot gas stream, ensuring an adequate concentration of scattering centers of suitable size and elimination of the effects of vibration and strong magnetic fields.

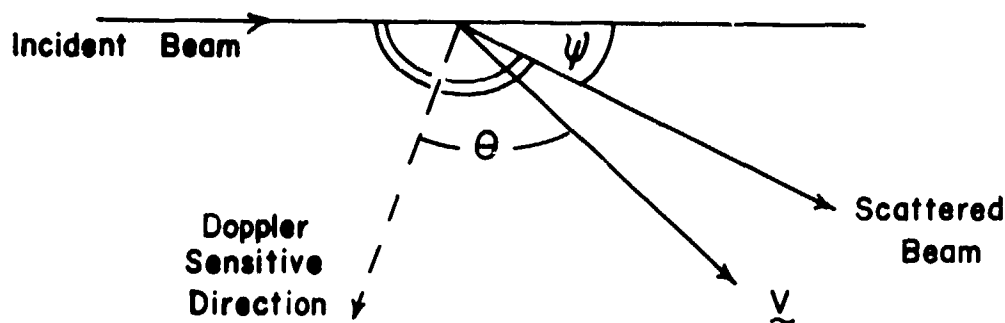
In the following sections we report the design and preliminary testing of a laser doppler velocimeter to satisfy these requirements.

#### 4.2. 2. Basic Design Considerations

In this section we outline the basic considerations leading to the choice of configuration discussed in detail later.

##### (a) Scattering Geometry

The first basic choice concerns the scattering geometry.



Particle Scattering Geometry

Figure 8

For the general geometry of Fig. 8, the frequency shift  $\delta \nu$  is given by

$$\frac{\delta \nu}{\nu} = 2 \left( \frac{v}{c} \right) \cos \theta \sin \frac{\psi}{2} . \quad (1)$$

For instance, for visible light  $\nu \sim 6 \times 10^{14}$  Hz, and taking  $\cos \theta \sin(\psi/2) \sim 1$ , then for a velocity  $v \sim 500$  m/sec, typical of the Stanford combustion MHD rig, we have  $\delta\nu \sim 2$  GHz, a microwave frequency.

In practice, the backscatter configuration,  $\psi = \pi$ , is very convenient, indeed virtually mandatory, since the same optics are used for the incident and scattered beams. In this way, alignment of these beams at a common point is automatically ensured, thus avoiding the difficult tracking problem involved in using separate optics for the two beams. The backscatter configuration is also economical on optical components and requires only a single viewing port into the MHD channel. Furthermore, the distribution of scattered power, according to the theory of Mie scattering from spheres, shows a relative maximum in the backscatter direction. On the debit side is the fact that the incident and scattered beams must be separated by a beam splitter, which wastes half the power in each beam. However, this power loss is acceptable. Another problem encountered with the backscatter configuration is that the power incidentally scattered and reflected back from the incident beam by the optical components, may give rise to a reference signal at the unshifted frequency which is too large compared with the signal scattered from moving particles. This difficulty may be overcome by polarization decoupling, as described later.

#### (b) Frequency Shift Measurement

There are two basic methods for measuring the frequency shift: optical heterodyning and direct spectral analysis using a high resolution Fabry-Perot interferometer. The former is relatively insensitive to frequency jitter and drift due to vibration and temperature changes, since the scattered signal is instantaneously mixed with a fraction of the incident signal.

In contrast the second method requires a high degree of frequency stability of both the laser and the interferometer. Unfortunately, optical heterodyning is limited by the frequency response of photomultipliers to shifts less than 500 MHz, thus restricting its use to low velocities. One possible way of circumventing this, in the backscatter mode, is to look almost normal to the flow, i.e.,  $\theta \approx 90^\circ$ . However this is undesirable because the system is then relatively more sensitive to turbulent velocity components along the line of sight. Furthermore, with finite apertures, the range of angles about  $\theta \approx 90^\circ$  causes serious degradation of velocity resolution. Possibly optical heterodyning to frequencies as high as 10 GHz could be accomplished using the latest, state-of-the-art fast photo-detectors. However these have low gain and would require wide-band amplifiers. For these reasons, it was decided to employ the second, direct method, and assume that the necessary frequency stability can be achieved.

The conventional Fabry-Perot interferometer consists of a pair of air-spaced, highly-reflecting, optical flats, aligned parallel to each other and normal to the light beam. It acts as a narrow band frequency filter, transmitting collimated light only when the plate separation  $t$  and wavelength  $\lambda$  satisfy the condition for constructive interference of the multiply reflected beams:

$$2t = n\lambda . \quad (2)$$

The frequency interval between successive modes,  $n$  ,  $n+1$  , is called the free spectral range  $\Delta\nu$  given by:

$$\Delta\nu = c/2t . \quad (3)$$

This is the maximum frequency difference that can be measured without ambiguity due to the multimode character of the device. The width  $\delta\nu$  to half-power of each mode is given by

$$\delta\nu = \Delta\nu/\mathcal{F} , \quad (4)$$

where  $\mathcal{F}$  is the finesse and is determined by the flatness of the plates and the reflectivity of the coatings. With high quality optical flats and coatings, values of  $\mathcal{F} \sim 100$  are attainable.

For the present purpose, we would choose the spacing  $t$  to give a free spectral range somewhat greater than the maximum frequency shift corresponding to the maximum velocity to be measured. For instance  $t = 7.5$  cm gives  $\Delta\nu \sim 2$  GHz. By arranging for a reference beam, as well as the scattered beam, to enter the interferometer, and by scanning the plate separation over a distance somewhat more than half a wavelength, transmitted signals may be displayed on a synchronously driven oscilloscope as shown in Fig. 9.

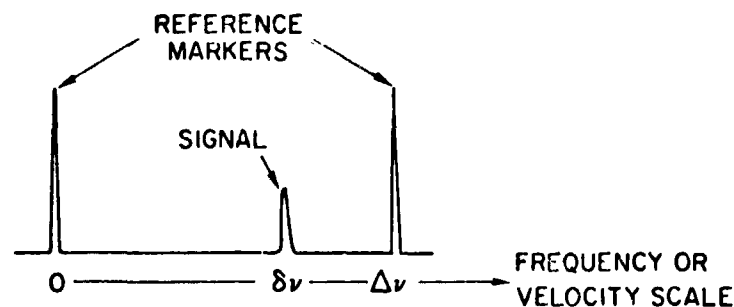


Figure 9  
Oscilloscope Velocity Display

The horizontal deflection corresponds to a linear frequency scale for the frequency shift  $\Delta\nu$  of the scattered light, with reference markers at zero frequency and at  $\Delta\nu$ , the latter being calculable from the known plate separation. It should be noted that if  $\nu$  exceeds  $\Delta\nu$ , the signal will appear at a position corresponding to the frequency  $(\nu - \Delta\nu)$ , so that there is ambiguity in the frequency shift to within an integral number of  $\Delta\nu$ . This is the reason why it is desirable to choose  $\Delta\nu$  somewhat larger than the maximum expected frequency shift. The velocity resolution, expressed as a percentage of the maximum velocity corresponding to  $\Delta\nu$ , is then  $(100/f)\%$ , so that a velocity resolution of the order of 1% is possible.

Recently, piezo-electrically scanned Fabry-Perot interferometers using spherical mirrors spaced confocally, have become commercially available. These have a number of advantages over the planar type, including lower cost, higher finesse and, most importantly, a greater light gathering power (étendue) when used with well-collimated narrow beams. This latter feature is particularly appropriate for the optical configuration considered below, in which the scattered beam is compressed by reverse passage through the same telescope that is used to expand the incident beam. The only disadvantage of the confocal Fabry-Perot is that the free-spectral range is not adjustable, being fixed for a given pair of mirrors by the confocal spacing condition. However, various free spectral ranges in the range 1 - 10 GHz can be obtained by inserting different mirror sets into the same housing. Typically a finesse of 300 is achieved in the visible, corresponding to a velocity resolution of 0.3% of the maximum velocity. This is more than adequate for our purpose.

In the case of the confocal Fabry-Perot, formulae (2) and (3) are modified to

$$4r = n\lambda \quad (2a)$$

and

$$\Delta\nu = c/4r \quad (2b)$$

where  $r$  is the radius of curvature of the mirrors and equals their spacing.

### (c) Beam Focusing and Spatial Resolution

Lasers operating single-mode in the visible spectrum typically produce an output beam with a gaussian intensity profile of width to  $1/e^2$  points  $\sim 1$  mm and with spherical wavefronts corresponding to a divergence half-angle of  $\sim 10^{-3}$  radian. To obtain the required spatial resolution this beam must be focused.

Now if a gaussian beam is focused by an aberration-free lens (or mirror), then the intensity profile remains gaussian and is given by:

$$I(r,z) = \frac{2 P_0}{\pi a^2(z)} \exp - 2 \left( \frac{r}{a(z)} \right)^2, \quad (5)$$

where  $P_0$  is the total power and the radius  $a$  (to  $1/e^2$  point) is given by:

$$a(z) = a_s \left[ 1 + \left( \frac{\lambda z}{\pi a_s^2} \right)^2 \right]^{1/2}. \quad (6)$$

Here  $z$  is measured from the focal plane where the beam has its minimum radius  $a_s$ .

If a collimated beam of diameter  $2 a_b$  is focused by a lens of focal

length  $f$ , as shown in Fig. 10,

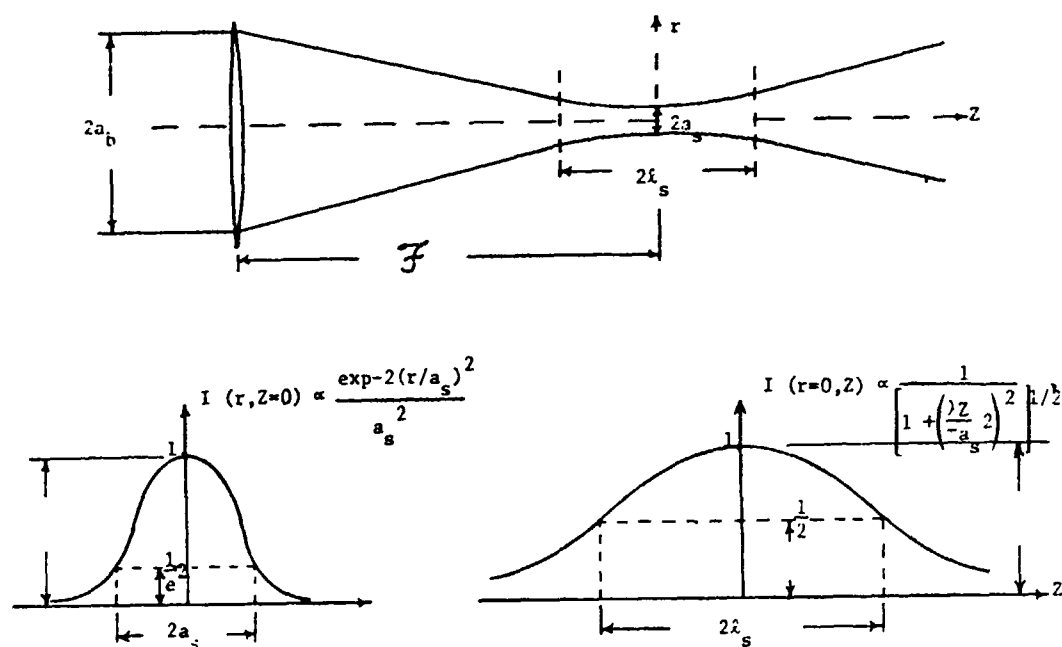


Figure 10  
Beam Focusing Diagram

we have from Eq. (6):

$$2a_s = \frac{4}{\pi} \frac{f\lambda}{2a_b} = \frac{4}{\pi} F\lambda, \quad (7)$$

and

$$2l_s = \frac{2\pi a_s^2}{\lambda} = \frac{8}{\pi} F^2 \lambda, \quad (8)$$

where  $l_s$  is the axial distance to the half-intensity points and  $F \equiv f/2a_b$  is the effective numerical aperture of the lens. It should be noted that away from the focal spot, the intensity falls off much less rapidly in the axial direction than in the radial direction, and, except in the

limit of  $F/1$  optics, the length of the focal region is greater than its diameter (by a factor  $\sim 2F$  ).

Physical restrictions set by the geometry of the Stanford M.H.D. rig prevent our putting a focusing lens closer than about 50 cm from the observation point, i.e.  $f \geq 50$  cm . If the laser beam were directly focused by a lens of this focal length, we should have  $F \sim 500$  , and hence a focal region of diameter  $2a_s \sim 0.3$  mm and length  $2\ell_s \sim 15$  cm . This is much too large for our purpose and we are led to consider expanding the beam to a larger diameter before focusing it. Diffraction-limited (i.e. aberration-free) beam-expanding telescopes for use with visible lasers are commercially available with expansion factors, depending on choice of lenses, up to 50 times. They consist of an input beam-expanding lens (effectively a microscope objective) and a large diameter collimating lens combination or telescope objective designed for minimum spherical observation.

Using such a beam-expanding telescope, our basic optical configuration then appears as shown in Fig. 11.

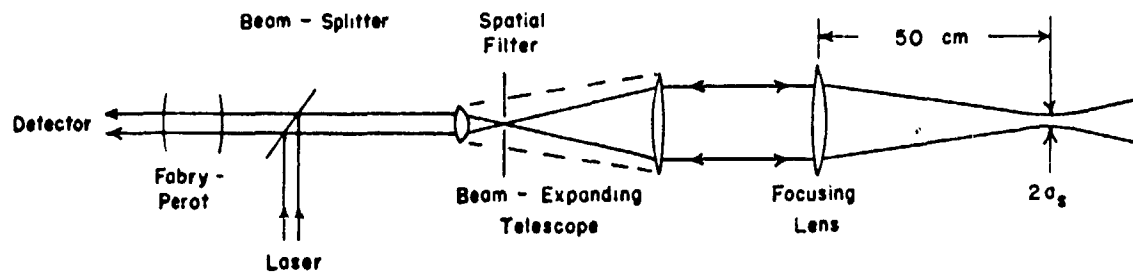


Figure 11  
Optical Configuration



It should be noted that the focusing lens also acts as the collecting lens for scattered light, which is compressed into a narrow beam,  $\sim 1$  mm diameter, for acceptance by the Fabry-Perot. The choice of beam expansion factor, and hence the numerical aperture of the focusing lens, determines not only the dimensions of the focal volume, and hence the spatial resolution, but also the collection efficiency. The latter improves as the aperture is increased ( $F$  decreased), but a limit is set by the degradation in velocity resolution produced by the range of angles  $\theta$  involved in the finite aperture.

Differentiating Eq. (1) gives the relative spread in apparent velocity, due to the finite aperture as:

$$\frac{d(\delta v)}{\delta v} = \tan \theta \, d\theta = \frac{\tan \theta}{2F} . \quad (9)$$

The angle  $\theta$  between the beam axis and the channel axis is determined by geometrical considerations as  $\theta = 26^\circ$ , as discussed later.

In practice, the beam expansion factor was chosen to be a factor  $\sim 50$ , the maximum readily available, corresponding to an expanded beam diameter of 50 mm and a numerical aperture of  $F \approx 10$  for the focusing lens. This is consonant with considerations of the geometry of the window and port into the M.H.D. channel. Eq. (6) then leads to an apparent frequency spread, due to finite aperture, of  $\sim 2.5\%$ . In practice, taking account of the energy integrated over the focusing lens area, we should find a relative velocity resolution somewhat less than this, say 2% at most.

The dimensions of the focal volume calculated from Eqs. (7) and (8) are then  $2a_s \approx 7\mu$ ,  $2\ell_s \approx 140\mu$ , which should give excellent spatial resolution for our purposes. It may be noted that the velocity resolution could

be improved, at the expense of reduced spatial resolution, by using a smaller beam expansion factor (by changing the expanding lens in the telescope), but it should be remembered that the signal pulse amplitude, its duration and the rate of acquisition of scattered signals are all affected by such changes.

The final matter to be discussed under the heading of spatial resolution is spatial filtering. By placing a pinhole at the focus of the beam-expanding lens, i.e. at the cross-over in the telescope, one can discriminate against the detection of light originating outside the focal volume of the focusing lens. This not only sharpens the spatial resolution for scattered laser light (especially in the axial direction), but discriminates against the detection of radiation from the hot gas and, more especially, from the hot electrode, particularly when probing very close to the latter. Rejection of the radiation background is also achieved by using a narrow band filter ( $\sim 10 \text{ \AA}$ , centered on the laser line) in front of the detector, but spatial filtering is also effective and desirable. Spatial filters, in the form of a pinhole with accurate  $x$ ,  $y$ ,  $z$  position controls, are supplied as accessories to beam-expanding telescopes. By using a pinhole somewhat larger than the theoretical cross-over diameter, one can clean up any wavefront distortion, either inherent in the laser output, or introduced by imperfections in the beam-expanding lens. Thus the spatial filter serves the double purpose of maintaining wave-front purity in the incident beam, and discrimination against signals from outside the focal volume in the collected beam.

#### (d) Laser Source Requirements

For proper functioning of the velocity analyzer, it is clearly necessary that the laser source should operate single-mode. Furthermore it is clear that because of the very small focal volume, necessitated by the high

spatial resolution required, then, for any realizable particle concentration in the flow, the probability of finding a particle in the focal volume at any instant is much less than unity. Consequently we have to detect individual pulses scattered by single particles as they pass through the focal volume. For instance, for a focal volume of cross-sectional area projected normal to the flow of  $10^{-5} \text{ cm}^2$ , a flow velocity of 500 m/sec, and a particle concentration of  $10^3 \text{ cm}^{-3}$  (1 mm average spacing between particles), we shall have  $\sim 500$  particles passing through the focal volume per second. However, because the Fabry-Perot scans with a frequency (velocity) bandwidth only  $\sim 1\%$  of the frequency (velocity) excursion, we shall detect only  $\sim 1\%$  of these, i.e.,  $\sim 5$  particles/sec for these conditions.

The problem thus comes down to the detectability of such pulses against the noise background which in this case, assuming negligible background radiation is admitted to the detector, consists of the dark current pulses of the photomultiplier. The amplitude of the signal pulses is proportional to the laser power level and the scattering cross-section of a particle, as well as the collection and transmission efficiencies of the optics. Clearly, in view of the low rate of acquisition of signals, it is desirable to use a continuously operating laser, rather than a pulsed one, provided sufficient power can be obtained in the continuous mode to give detectable signals from the size of particles considered.

Since the quantitative evaluation of these factors, involved in signal detectability, is subject to considerable uncertainty, it is best to rely on performance data from previous work. With a laser doppler velocimeter rather similar to that considered here, Seifert was able to detect signals from particles in the size range  $1 - 10 \mu$  in solid fuel rocket exhausts,

using a continuous, single-mode He-Ne laser with an output of  $\sim 100 \mu$  watts. However, at the lower size limit ( $\sim 1 \mu$ ) the signal/noise ratio was marginal and he had to resort to dividing the scattered light between two photomultipliers and using a coincidence circuit to improve the detection of signals against the random dark current pulse background.

For these reasons it seemed desirable to use an Argon ion laser, which is the only convenient alternative, and which delivers some 100 m watts single mode on either a green line (5145 Au) or a blue line (4880 Au). This gives a factor  $10^3$  in power compared with the He-Ne laser and furthermore, one also gains from the higher quantum efficiency of photocathodes in the blue-green compared with the red.

The only disadvantage of the  $A^+$  laser compared with the He-Ne one, is that, because of the much higher discharge power, the amplitude and frequency stability is somewhat poorer. The principal effect is low frequency (a few Hz) modulation of the laser frequency due to mirror vibration induced by turbulence or local boiling in the water cooling jacket. The frequency jitter is of the order  $\pm 20$  MHz, which causes some degradation of the velocity resolution due to jitter (along the horizontal axis) in the display (Fig. 2) over times of the order of 0.1 secs. Whether this is important depends on how long the display must be stored before recording, which in turn depends on the signal acquisition rate. If the latter is high enough, the display can be stored for a time short compared with the characteristic jitter time, in which case the jitter is unimportant.

#### (e) Detection, Display and Recording

The signals to be detected consist of reference signals and scattered signals whose characteristics we consider in turn. Ideally, the amplitude

of the reference signals should be of the same order or somewhat larger than the scattered signals, which themselves should be at least an order of magnitude than the noise level. On first testing the system in the back-scatter configuration shown in Fig. 11, it was found that the reference signal due to reflection at the (anti-reflection coated) surfaces of the beam-expanding lens, together with light scattered from the edges of the pinhole, constituted a reference signal which was much too large--some three orders larger than noise. To reduce this level, without affecting the scattered signal level, use was made of a polarization decoupling scheme. A horizontally-oriented polarizer was introduced in front of the Fabry-Perot. Since the laser output is vertically polarized this rejects the reference signal. A quarter wave plate, designed for  $\lambda = 5145 \text{ \AA}$ , was placed between the telescope objective and the focusing lens, so oriented to produce circularly polarized light in the probing beam. Scattered light which is likewise circularly polarized, is converted to a horizontally polarized signal on reverse passage through the quarter wave plate, and passes the horizontal polarizer to be detected. In this way the amplitude of the reference beam was reduced by some 20 db (i.e. two orders) relative to the signal.

The pulse length of the reference signal is determined by the bandwidth of the Fabry-Perot together with its scanning rate. The scan-rate cannot exceed about 1 kHz if the mirrors are to faithfully follow the sawtooth waveform, and in practice a time of  $\sim 10 \text{ m sec}$  to scan over one free-spectral range was found to be convenient. For a finesse of  $\sim 100$ , this gives a reference signal pulse length of  $\sim 100 \text{ } \mu\text{sec}$ . Such pulses will write quite satisfactorily on a synchronously driven scope with a time base of  $10 \text{ m sec}$ .

By comparison, the scattered light pulse due to passage of a single particle through the focal volume is of very short duration,  $\sim 50$  n sec for the conditions envisaged, and at the lower limit of particle size ( $\leq 1 \mu$ ) may contain only of the order of 10 photons. The most convenient and versatile detector is a photomultiplier, since it is fast and has high gain, capable of detecting such pulses and amplifying them to a level at which they can be recorded.

For instance, the 14-stage RCA 7205 with S.20 cathode has a quantum efficiency of 12% at 5145 Å, a rise time of 3 n sec, and a current gain of  $5 \times 10^7$  when operated at 2400 V. Thus, using a 50  $\Omega$  output cable terminated in 50  $\Omega$ , one can expect to reproduce pulses as short as 10 n sec, consisting of only a few photoelectrons, and amplify them to a level  $\sim 100$  m V, which is adequate as input to a broad-band (30 MHz) oscilloscope amplifier. It is desirable to be able to record individual scattered light pulses without loss of time resolution, since it gives an independent check on the effective size of the focal volume actually achieved. However it is generally difficult or inconvenient to record such fast pulses photographically from an oscilloscope and, except when investigating the pulse length, it is desirable to lengthen the pulses so that they write more effectively on the oscilloscope screen. This can be done most easily by using a much larger load resistor, so that the time constant formed with the output capacity of the photomultiplier, together with that of the cable, is long enough for effective writing. At the same time the photomultiplier gain is reduced by lowering the operating voltage, to avoid saturation effects.

For a velocity display as shown in Fig. 9, it is desirable to increase

the detector time constant until it is comparable with the pulse length ( $\sim 100 \mu \text{ sec}$ ) of the reference signals as given by the Fabry-Perot bandwidth and scan rate. The writing efficiency is then comparable for the scattered and reference signals when these are of comparable amplitudes.

The noise background, against which the signal pulses must be detected, consists of the so-called random dark current pulses. These arise from thermionic emission from the cathode, from secondary emission from the electrodes due to ion bombardment, and from cold emission from electrodes. While the pulses originate primarily from single electron emission events, the anode pulses vary in height due to the varying statistics of the multiplication process. The average frequency of such pulses is not normally quoted, but may be estimated from the manufacturer's specification. From the average anode dark current (at  $22^\circ \text{C}$ ) and the gain, we obtain an equivalent cathode dark current  $\sim 10^{-14} \text{ A}$ , corresponding to some  $5 \times 10^4$  electrons/sec randomly generated at the cathode. The frequency of such pulses may be reduced by cooling the photomultiplier with dry ice, which eliminates the thermionically emitted component, but there is an irreducible minimum pulse rate of  $\sim 10^4/\text{sec}$ .

To detect signal pulses with reasonable certainty against this background, either they must be significantly larger than the dark current pulses or they must occur significantly more frequently. We have seen that, in view of the small focal volume, it is unlikely, for reasonable particle concentrations, that we shall have a signal rate of more than  $\sim 10$  per second. Consequently the second alternative is not open to us, and it is essential that the signal pulses be larger than the dark current-pulses, containing, say, at least 100 photons (12 photo electrons) per

pulse. This sets a limit on how small a particle can be detected.

In section 4 we make some rough calculations of the amplitude of the detected signals for our particular instrument design, and show that we may expect  $\sim 10^3$  photons per pulse for  $1 \mu$  particles. It should be emphasized, however, that this is a very rough estimate and that the performance of the system can only be reliably determined from measurements using particles of known size.

If, for some reason, the signals are not so much larger than the dark current pulses that they can be unambiguously distinguished, then it is still possible to distinguish them, even though they occur much less frequently than the dark current pulses, by dividing the signal between two photomultipliers with fast response, followed by a coincidence circuit. Hopefully our signals will be large enough that we shall not need to resort to this degree of sophistication. The primary mode of operation uses a velocity display as shown in Fig. 9. Since the scan period is  $\sim 10$  m sec, while the signal rate is anticipated to be only  $\sim 10$  per second, it is clear that, in general, we shall need to scan continuously and store signals for the order of one or more seconds. This may be done photographically, using a suitably long exposure, but a more convenient method is to use a storage oscilloscope. In this way a suitable result is obtained before recording it permanently on film.

#### 4.2.3. Detailed Design Considerations

Having determined the basic design parameters of the velocimeter, we now discuss some detailed matters related to constructing an instrument capable of making the required measurements on the Stanford combustion



MHD rig. The latter imposes quite severe constraints concerning access to the measurement region, vibration isolation and magnetic shielding. First, we consider the question of access to the measurement region.

(a) Access Port, Scan Mirror and Focusing Lens

The main MHD channel is some 60 cm long and situated in a uniform magnetic field of some 3 Tesla provided by a large electromagnet. The channel is constructed of double-walled, stainless steel incorporating a water cooling jacket, lined with MgO firebrick, and has internal dimensions 10 cm high by 3 cm wide. It is required to make measurements adjacent to an electrode (3 cm wide x 2 cm long) in the top surface of the duct and positioned near the downstream end of the main channel, where the boundary layer is fully developed.

The access port must transmit the probing beam which consists of a converging conical pencil of half-angle  $\sim 3^\circ$ , corresponding to F/10 optics. It must also accommodate the beam, without vignetting, as it is deflected vertically to move the focal point from the electrode surface to some 2 cm below it into the free stream.

The design adopted, shown in plan in Fig.12 gives access through a side wall downstream of the measurement point. This minimizes perturbation of the boundary layer at the electrode by the discontinuity in the side wall. The angle  $\alpha$ , in the horizontal plane, between the beam and channel axes was set at  $26^\circ$  by geometrical considerations. This gives a reduction factor  $\cos \alpha \approx 0.90$  in Eq. (1) relating the frequency shift to the velocity. Considering the vertical section through the beam and port axis, shown in Fig.13, it is clear that the most critical factor is to ensure that the convergent pencil can be focused at the center of the

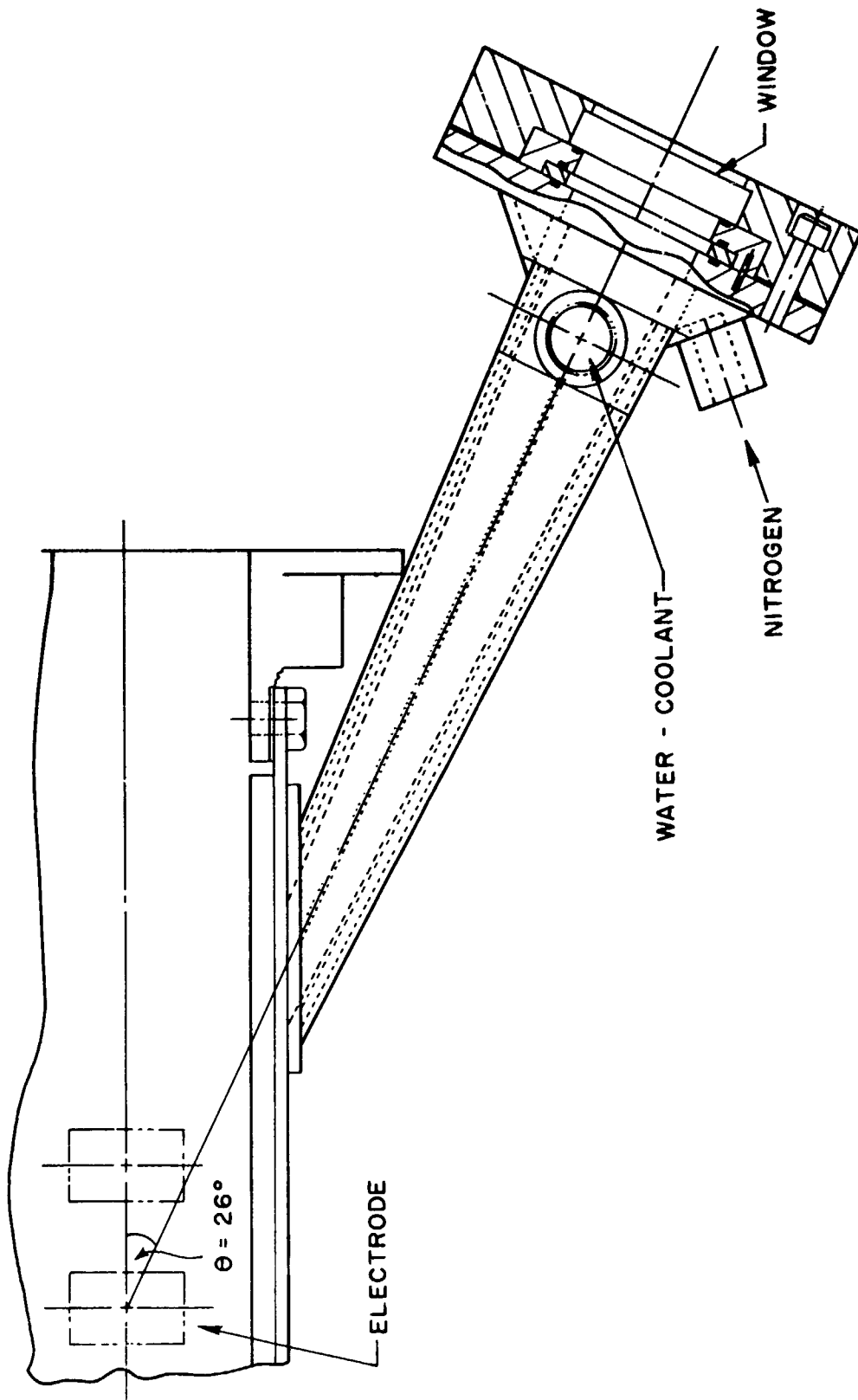


Figure 12 Plan View of Port

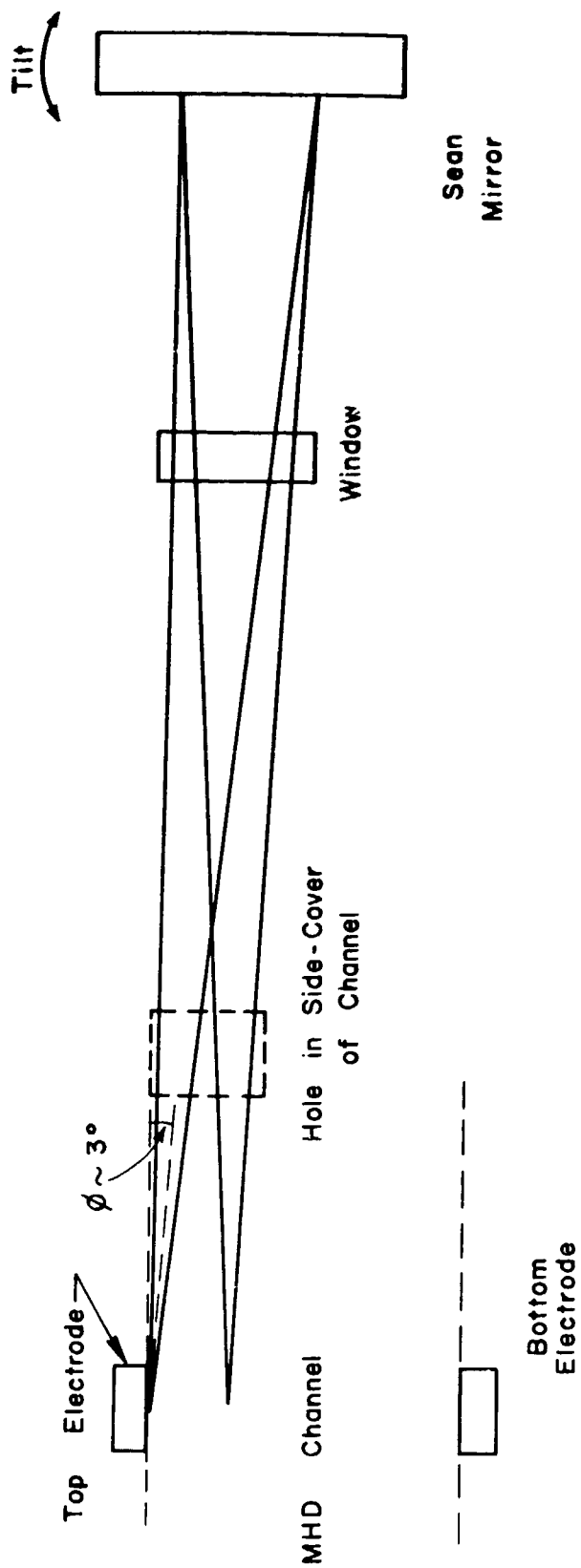


Fig.13. Vertical Section through Port

electrode surface without vignetting anywhere on the port . channel walls. This was accomplished by making the angle  $\theta$  , between the horizontal and the axis of the beam (when focused on the electrode) slightly greater than the half-angle of the convergent cone. The upper edge of the cone then just clears the electrode and firebrick surfaces.

The length of the port was made as long as possible (~12 in) consistent with not obtruding into the space required to locate the scan mirror, so as to protect the window as far as possible from the hot gas flow. The port walls were constructed of a double layer of stainless steel spaced by a water cooling channel, and the whole assembly welded to the side cover of the main channel. The window, consisting of a 2" dia x 1/2" thick fused silica optical flat ( $\lambda/20$ ), was sealed to the port with an O-ring, and provision was made to direct a stream of nitrogen onto its inner surface. The nitrogen flow was designed to inhibit the entry of hot gas into the port. However the flow must be maintained at a moderate level lest it perturb the boundary layer at the measurement point.

To keep the diameters of the scan mirror and focusing lens of reasonable size, it is necessary to position them as near as possible to the measurement point. Of the two possible configurations of scan mirror and focusing lens, corresponding to deflection before or after focusing, the latter arrangement was adopted, since the former would involve using the lens off-axis and thus give rise to coma in the focal "spot". The scan mirror, consisting of a 3" dia x 3/4" thick glass optical flat ( $\lambda/20$ ) is positioned and oriented so as to deflect the beam, incident from a direction normal to the channel axis, centrally into the port. Its front surface is dielectric-coated for maximum reflectance at this angle at

$\lambda = 5145 \text{ \AA}$ . The poor reflection at other wavelengths minimizes the collection of radiation from the gas or walls. Scanning of the focal spot in the vertical direction is accomplished by tilting the mirror mount about a horizontal axis in the plane of the mirror surface. This motion is controlled by a micrometer positioned 3 in from the tilt axis. Since the distance from the mirror to the focal spot is  $\sim 21$  in, there is a lever arm magnification of seven times between the movements of the focal spot and the micrometer.

The focal length of the focusing lens should be chosen to be the minimum consistent with locating it close to the scan mirror, so as to preserve maximum aperture. This resulted in the value  $f = 56 \text{ cm}$ , which, in view of the maximum diameter (50 mm) of the expanded beam set by the telescope aperture, corresponds to  $F/11$ . It proved impossible to find a diffraction-limited lens (as opposed to an ordinary achromat) with these approximate characteristics, except as a special order. Eventually, a 60 mm diameter diffraction-limited air-spaced doublet with  $f = 54 \text{ cm}$  ( $F/9$ ) was located. This focal length is too short, and with a collimated beam from the telescope would put the focal spot some 2 cm short of the electrode center. However, by defocusing the telescope, to produce a slightly divergent beam ( $\sim 0.1^\circ$  half-angle), it is possible to bring the focal spot to the required position. While the telescope and focusing lens are designed for zero spherical aberration for collimated beams, the degradation produced by this slight departure from exact collimation is quite negligible.

(b) Layout and Mounting of Optical System

While the scan mirror and focusing lens must be mounted close to the port, there is some choice possible in locating the rest of the optical

system. From the point of view of minimizing the magnetic shielding problem, and, possibly, also the vibration isolation problem, it would be desirable to mount the rest of the system on a stable platform well removed (say 5 meters) from the MHD rig. However, the operator must be able to set and read the scan mirror micrometer as well as make adjustments to the laser and electronics while observing the oscilloscope display. Consequently, a remote location would necessitate an accurate remote drive and sensing mechanism for the scan mirror. For these reasons a compact layout was adopted, as shown in Fig. 14, whereby all the controls are within reach of a single operator.

The optical system is mounted on a rigid framework formed of two 4 in aluminum H-beams, bolted at right angles and cantilevered from the iron core of the electromagnet. Since the latter weighs some 10 tons and rests firmly on the reinforced concrete floor, it was judged to form a stable support. The free ends of the H-beams are supported by surveyor's tripods. This system has the advantage that the framework can be readily removed and used to support the optical system in an alternative location, namely a darkroom, for preliminary testing. With the exception of the laser, which rests directly on the H-beam, all the optical components, including the focusing lens and scan mirror, are mounted, using standard optical carriages and adjustable mounts, on an optical bench which is rigidly bolted to the H-beam. This greatly facilitates alignment of the optics.

It was necessary to screen both the laser and the photomultiplier from the stray magnetic field from the electromagnet, whose magnitude was ~1000 oersted at each location. While the laser operates in an axial field

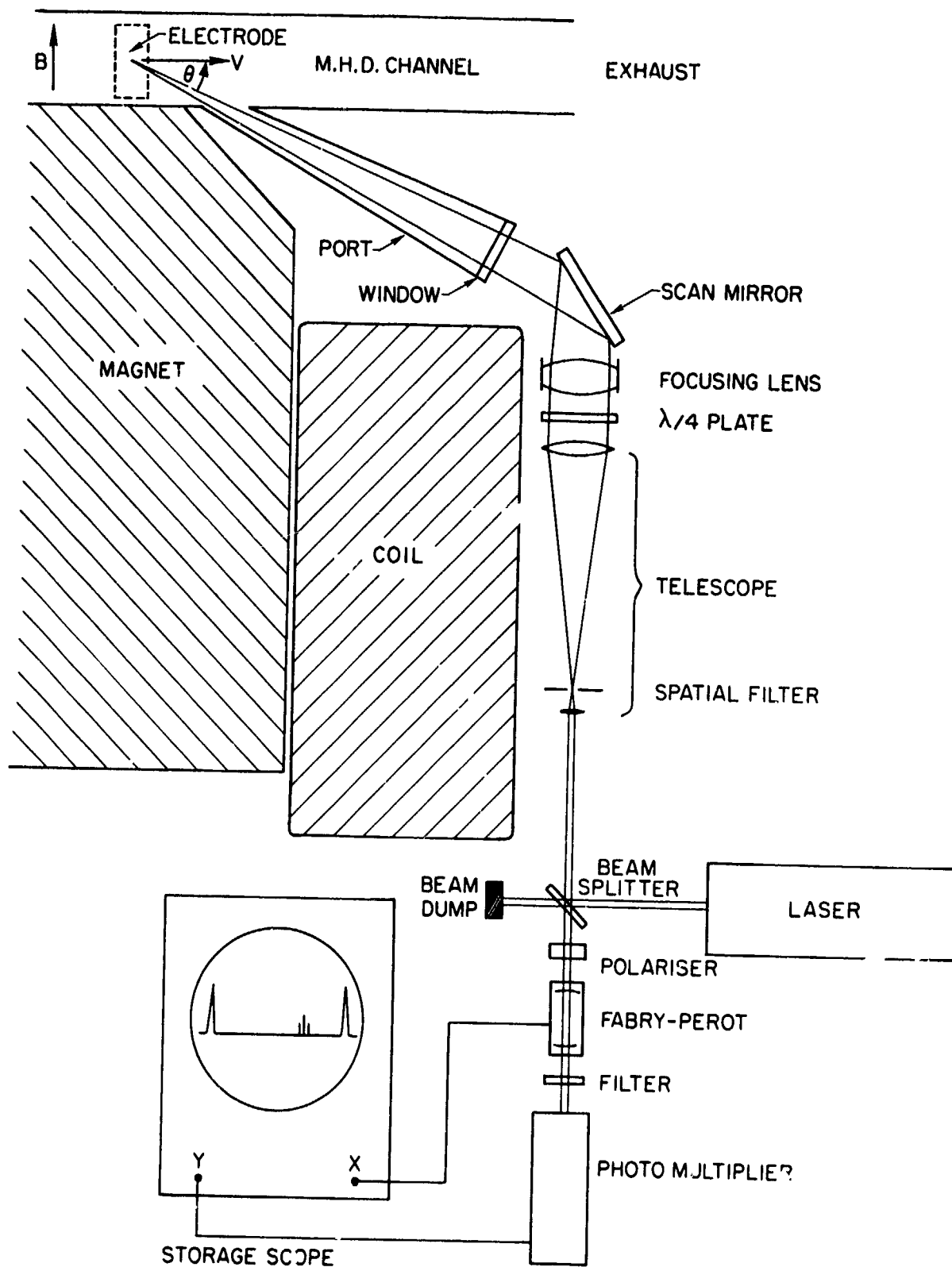


Figure 14 Optical Layout

of ~800 oersted, it is adversely affected by transverse fields of more than a few oersted. Adequate shielding was provided by surrounding the laser with an open-ended box constructed of 1/8" thick mild steel. The functioning of the photomultiplier is likewise adversely affected by fields of a few oersted. Adequate shielding was provided by surrounding the tube by a length of thick-walled (1/4") iron pipe. All the components of the optical system are constructed of non-magnetic material, with the exception of the micrometers controlling the tilt motions of the optical bench mounts. The force exerted on the micrometers could possibly cause misalignment of the optics during operation when the magnetic field is changed. In practice, the only noticeable effect was a deflection of the focal spot due to strain induced in the mount of the scan mirror. This could be corrected by re-setting the micrometer (by 0.004"), but a better solution would be to replace the micrometer by a non-magnetic one.



#### 4.2.4 Component Specifications and System Characteristics

The specifications of the optical components selected for the final design are listed in Table I.

TABLE I

Laser Power, Single Mode (5145 Au)	$P_o$	$10^{-1}$ w
Output beam diameter	$2 a_L$	1.1 mm
" " divergence		$9 \times 10^{-4}$ radian
Transmission of Beam-Splitter	$T_B$	50%
Telescope expanding lens, focal length	$f_E$	6.1 mm
" " " aperture	$2 a_E$	1.7 mm
Spatial filter, pinhole diameter	$2 a_{ph}$	15 $\mu$
Telescope collimating lens, focal length	$f_T$	200 mm
" " " aperture	$2 a_T$	50 mm
Transmission of Telescope and Spatial Filter	$T_T$	70%
Transmission of Quarter-wave plate	$T_Q$	85%
Focusing Lens, focal length	$f_F$	54 cm
" " aperture		60 mm
" " transmission	$T_F$	95%
Scan Mirror, Reflectivity	$R_M$	99%
Window transmission	$T_W$	90%
Numerical Aperture of Collection optics	F	11
Fabry-Perot--Free Spectral Range	$\Delta\nu$	2 or 8 GHz
" " Finesse	$\mathcal{F}$	$\sim 300$
" " Resolution	$d\nu$	7 or 27 MHz
" " Entrance Pupil		2 mm
" " Scan Period	T	$10^{-2}$ sec
" " Transmission	$T_{FP}$	50%
Polarizer, Max. Transmission	$T_P$	90%
Filter Transmission	$T_f$	50%
Photomultiplier, Quantum Efficiency	$\eta$	12%
" " Current Gain at 2400 V		$5 \times 10^7$

From these specifications, together with some nominal values for the flow conditions, we can now detail some calculations of the anticipated system characteristics. The figures are rough estimates and probably optimistic, particularly with regard to the magnitude of the detected scattered signal. However, a more accurate evaluation is hardly feasible and the true performance must be determined experimentally. Nevertheless the calculations are useful to illustrate the functional dependence of the performance on the external parameters of the design. The principal results are listed in Table II. Some comments on the various entries follow:

- (3,4,5) The particle diameter and concentration assumed have been taken as about the smallest with which we can reasonably work. Under these conditions, the volume flow of particulate matter is quite low ( $10^{-3} \text{ cm}^3/\text{sec}$ ) but would become appreciable ( $1 \text{ cm}^3/\text{sec}$ ) if  $d$  were increased to  $10 \mu$  or  $n$  increased to  $10^6 \text{ cm}^{-3}$ .
- (6) The input beam almost exactly fills the telescope entrance pupil.
- (7) The pinhole was chosen to be five times the theoretical cross-over diameter.
- (8,9) The telescope objective is slightly overfilled and the expanded beam diameter is determined by the aperture of the objective.
- (10) By ray optics, the path of any light capable of being detected must pass through this image circle.
- (11,12) The focal volume is represented as a cylinder with uniform illumination within it and zero outside.
- (14) The angle  $\phi$  is taken when the focal spot is at the electrode surface.
- (17) This velocity resolution is determined by the finite aperture and not by the bandwidth of the Fabry-Perot, which is relatively smaller.

TABLE II

1. Channel Cross-section	A	30 cm <sup>2</sup>
2. Flow Velocity	v	500 m/sec
3. Particle Diameter	d	1μ (10 <sup>-4</sup> cm)
4. Particle Concentration	n	10 <sup>3</sup> cm <sup>-3</sup>
5. Volume Flow of Particulate	Avnd <sup>3</sup>	10 <sup>-3</sup> cm <sup>3</sup> /sec
6. Beam Diameter at Telescope Entrance	2a <sub>L</sub> '	1.65 mm
7. Diameter of Cross-over in Telescope	2 a <sub>x</sub>	3μ
8. Beam Expansion Factor	M = f <sub>T</sub> /f <sub>E</sub>	33
9. Expanded Beam Diameter	2a <sub>b</sub> = M.2a <sub>L</sub>	50 mm
10. Diameter of Pinhole Image at Focus	2a <sub>ph</sub> ' = 2a <sub>ph</sub> f <sub>F</sub> /f <sub>T</sub>	40μ
11. Diameter of Focal Volume	2a <sub>s</sub> = (4/π) f <sub>F</sub> λ/2a <sub>b</sub>	7μ
12. Length of Focal Volume	2ℓ <sub>s</sub> = 2π a <sub>s</sub> <sup>2</sup> /λ	0.15 mm
13. Angle between beam and flow axes, horizontal	θ	26°
14. Angle between beam and flow axes, vertical	φ	3°
15. Intercept of Focal Volume with flow axis	sℓ = 2a <sub>s</sub> /sin θ	16μ
16. Spatial Resolution normal to electrode	δy = (2a <sub>s</sub> + 2ℓ <sub>s</sub> sin φ)	15μ
17. Relative Velocity Resolution	(s <sub>v</sub> /v) = tan θ/2F	2%
18. Reference Pulse Length	τ <sub>R</sub> = T/4	30μ sec
19. Scattered Pulse Length	τ <sub>S</sub> = δℓ/v	30n sec
20. Area of Focal Volume normal to flow	A <sub>s</sub> = 2a <sub>s</sub> · 2ℓ <sub>s</sub> sin θ	5 × 10 <sup>-6</sup> cm <sup>2</sup>
21. Scattered Pulse Rate, gen.	v <sub>g</sub> = n A <sub>s</sub> v	250 sec <sup>-1</sup>
22. " " " det.	v <sub>d</sub> = v <sub>g</sub> δv/v <sub>max</sub>	5 sec <sup>-1</sup>
23. Power at Focus	P <sub>F</sub> = P <sub>O</sub> T <sub>B</sub> T <sub>T</sub> T <sub>R</sub> T <sub>M</sub> T <sub>W</sub>	2.5 × 10 <sup>-2</sup> w
24. Peak Scattered Power	P <sub>S</sub> = P <sub>F</sub> (d/2a <sub>s</sub> ) <sup>2</sup>	5 × 10 <sup>-4</sup> w
25. Collected Scattered Power	P <sub>C</sub> = P <sub>S</sub> /16 F <sup>2</sup>	2.5 × 10 <sup>-7</sup> w
26. Scattered Power to Photomultiplier	P <sub>PM</sub> = P <sub>C</sub> T <sub>W</sub> T <sub>M</sub> T <sub>T</sub> T <sub>B</sub> T <sub>F</sub> T <sub>P</sub> T <sub>F</sub>	1.4 × 10 <sup>-8</sup> w
27. Scattered Energy to Photomultiplier	E <sub>S</sub> = P <sub>PM</sub> τ <sub>S</sub>	4 × 10 <sup>-16</sup> J
28. Number Scattered Photons to Photomultiplier	N <sub>S</sub> = E <sub>S</sub> /hν	1000
29. Number Scattered Photoelectrons Generated	N <sub>P</sub> = η N <sub>S</sub>	120

- (19) This is the maximum pulse length for a particle passing through the axis of the focal volume.
- (22) Here  $v_{\max}$  is the maximum velocity corresponding to one free spectral range. For  $\Delta\nu = 2\text{GHz}$ ,  $v_{\max} = 570 \text{ m/sec}$ .
- (24,25) The scattering cross-section is taken as the projected area of the (spherical) particle and the scattering is assumed isotropic.

The aspect in which the actual performance is most likely to fall short of that calculated is probably the focal spot size. This is due to imperfections in the optical components. If the linear dimensions of the focal volume are in practice a factor  $\alpha$  larger than calculated, then the various performance factors scale in the following ways. The spatial resolution  $\delta y$ , the projected length  $\delta \ell$ , and the scattered pulse length  $\tau_s$  increase as  $\alpha$ . The projected area  $A_s$ , and the pulse rates  $\nu_g \nu_d$  increase as  $\alpha^2$ , while the scattered powers  $P_s$ ,  $P_c$ ,  $P_{PM}$  decrease as  $\alpha^{-2}$ . The scattered energy  $E_s$  and the numbers of photons  $N_s$  and photoelectrons  $N_p$  decrease as  $\alpha^{-1}$ .

#### 4.2.5 Alignment and Preliminary Testing

##### (a) Initial Testing of Laser and Fabry-Perot

As supplied, the laser operated multi-line and multi-mode and it was necessary to fit the prism and etalon supplied to convert it to single-mode operation. The prism is inserted into the optical cavity so that operation of the mirror vertical tilt control allows one to select one of the five lines in the blue-green. The etalon is also inserted into the optical cavity and, by adjusting its vertical and horizontal tilt controls, a single axial mode may be selected. The mode structure is illustrated in Fig. 15.

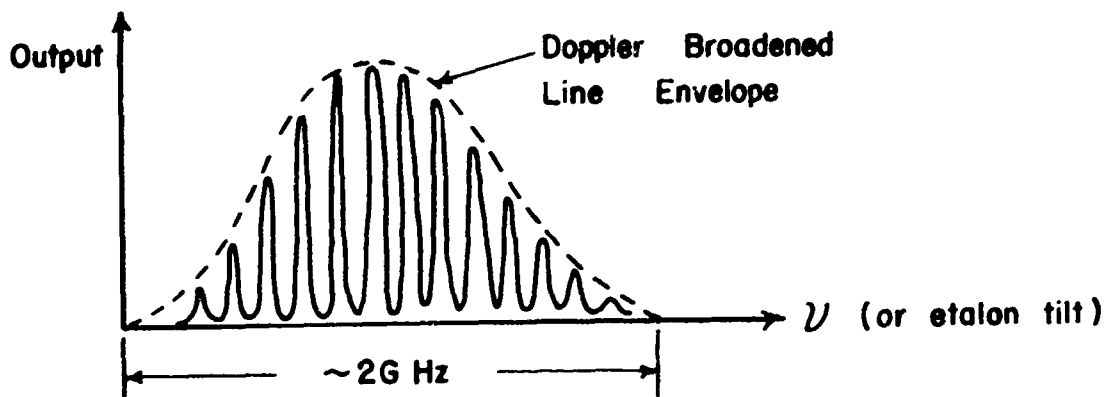


Figure 15

#### Laser Mode Structure

The exact position of the mode pattern within the line envelope depends on the length of the cavity and thus depends on the mirror settings and thermal tuning. Four adjustments, two for mirror tilt and two for etalon tilt must be made to obtain maximum output on the strongest mode (nearest to line envelope center). Considerable thermal instability, i.e., power variation, extinction and mode-hopping, occurs on first switching on, but after a prolonged warm-up (~ 2 hours) the laser operates stably on a single mode for periods of 10 minutes or more without adjustment of the controls.

The Fabry-Perot was set up in the scanning mode with a period  $T = 10$  m sec and synchronized to an oscilloscope. Initially it was driven from a separate ramp generator but, because of problems experienced with this, a drive from the oscilloscope time-base was substituted, using the circuit of Fig.16 to control the amplitude and provide a d.c. bias. Use of the same waveform for the time-base and scan drive minimizes effects due to nonlinear waveforms.

To align the Fabry-Perot and test the frequency stability of the laser relative to it, a small fraction of the output beam was directed into the

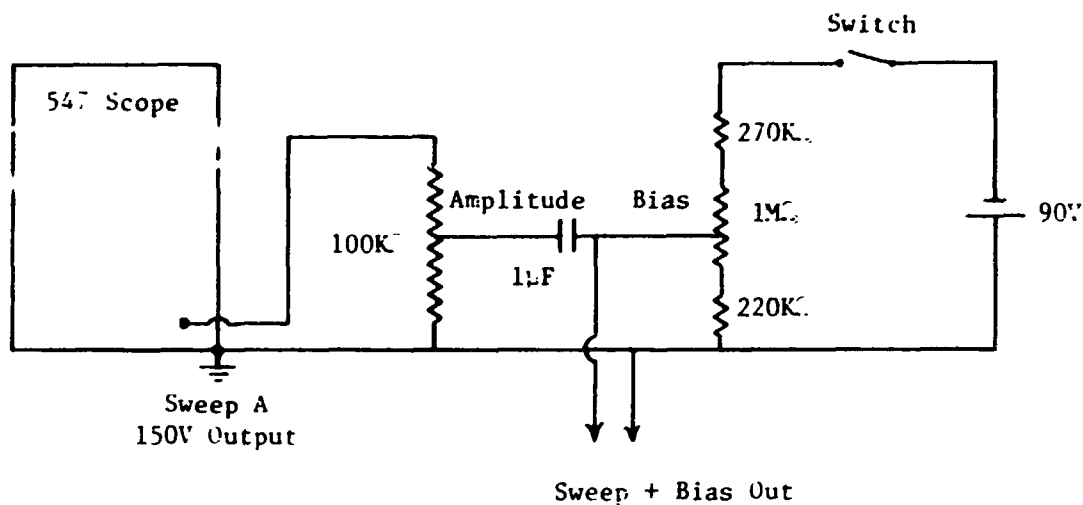


Figure 16  
Fabry-Perot Drive Circuit

Fabry-Perot using an uncoated optical fl<sup>a</sup> as mirror and the photodiode provided with the Fabry-Perot as detector. The spacing of the mirrors (2 GHz etalon) was critically adjusted, and the orientation of the interferometer relative to the beam set to give the sharpest response. A half-width of  $< 10$  MHz corresponding to a finesse of  $> 200$  was obtained.

By observing the steadiness of the oscilloscope display with the scan amplitude set to display two successive Fabry-Perot modes (one free spectral range) as in Fig. 9, it was possible to determine the frequency stability of the laser relative to the Fabry-Perot. The display drifts slowly due to thermal turning (primarily of the laser) and exhibits a short-term jitter at a few Hz due to vibration of the laser. Once the system is thoroughly warmed up, the thermal drift is within acceptable bounds, there being negligible drift (i.e., less than the resolution) over times of tens of seconds corresponding to the maximum storage time anticipated (with the slowest pulse acquisition rate).

The short-term jitter causes an apparent broadening of the reference pulses when the display is stored for times  $\sim 1$  sec, compared with their width with single scans (10 m sec). With the two reference pulses conveniently separated by 8 cm in the display, the width increases from  $\sim 0.5$  mm on single scan to some 2 mm on storing for times  $\sim 1$  sec. This causes a degradation in velocity resolution from some 0.5% to some 2%. While this is acceptable, it would be preferable to eliminate it, and some attempts were made to do so. It appears that the laser mirror system has a natural resonance of a few Hz, which is excited by vibration. Even when mounted on a very stable table, so that externally induced vibrations are negligible, there is frequency jitter of the amount noted ( $\sim 40$  MHz total excursion). This is apparently excited by the turbulence in the cooling water channels. It was particularly noted that if the water flow was reduced below 2.5 gallons/min, the jitter increased, due to the audible onset of local boiling. Apart from maintaining a flow (3 gallons/min) large enough to prevent this, it seems there is little that can be done to reduce the frequency jitter, without a major redesign of the laser, or the addition of an elaborate feed-back stabilizing system. The mirror resonance at a few Hz is also readily excited by vibration of the laser mount, as could be observed by lightly tapping the stable table. In comparison the Fabry-Perot is much less sensitive to vibration.

(b) System Alignment

The procedure devised to align the system in the configuration of Fig. 14 consists of the following basic steps:

- (i) To make the beam axis coincident with the axis of the optical bench, use is made of the fact that the beam diameter almost exactly fills

the telescope entrance pupil. Thus, by sliding the telescope carriage along the bench and watching for vignetting of the transmitted beam, one has a sensitive criterion for the required alignment of the axes. One thus adjusts the position and height of the laser, together with the position and tilt micrometers of the beam splitter to obtain no vignetting as the telescope is slid along the length of the bench.

- (ii) The telescope focus adjustment is now set to give a collimated beam. This may be done with sufficient accuracy at the present stage by making the beam diameter intercepted on a distant target ( $\sim 5$  meters) equal to the diameter at the exit to the telescope.
- (iii) The next step is to obtain a reflected beam which accurately defines the optic axis on the detector side of the beam splitter, allowing for beam displacement by refraction at the beam splitter and polarizer. This is done by temporarily setting up a mirror (an uncoated optical flat) in a holder beyond the telescope. The (visible) beam reflected back through the telescope is split by the beam splitter, and the mirror mount is critically adjusted to send one beam exactly back on the incident laser beam. This can be judged very sensitively by blowing smoke into the beams and making the incident and returned beams coincident. The other beam, transmitted by the beam splitter then accurately defines the axis for detection.
- (iv) With the polarizer in position, the lateral and vertical position of the Fabry-Perot is now set so that the (visible) beam enters the entrance pupil of the Fabry-Perot centrally. Using the photomultiplier as detector and with the Fabry-Perot scanning, the orientation of the latter is adjusted to give the maximum sharp detected signal.



- (v) The next step is to adjust the polarization optics. The polarizer is oriented to minimize the detected signal, under which condition it gives maximum rejection for the vertically polarized laser output, and maximum transmission for a horizontally polarized signal. The quarter-wave plate is then mounted to the front of the telescope and oriented to give a maximum in the detected signal. The reflected beam, having passed twice through the quarter wave plate is now horizontally polarized.
- (vi) The spatial filter is now fitted into the telescope at its cross-over. Three critical adjustments, two for lateral position and one for axial position, are made to put the pinhole at the cross-over of the incident beam, as judged by the maximum uniform illumination in the transmitted (expanded) beam.
- (vii) At this stage the cross-over of the reflected beam will not lie exactly at the pinhole because the telescope is not precisely collimated. This is done by adjusting the telescope focus until the detected signal is maximized.
- (viii) The temporary mirror is now removed. The signal detected at this stage is small and constitutes the reference signal due to light incidentally reflected from the surfaces of the beam expanding lens, together with light scattered from the edges of the pinhole. To reduce the latter as far as possible, final critical adjustments are made to the pinhole position controls.
- (ix) The final steps involve putting the focusing lens and scan mirror in position and adjusting them to direct the convergent beam centrally through the window and port. This can be judged by observing through

the MHD channel with the exhaust section removed, and blowing smoke into the duct. The telescope focus and scan mirror vertical tilt are then adjusted to bring the focal spot exactly at the center of the electrode.

When the scan mirror tilt is set to put the focal spot exactly on the electrode surface, an increase in the detected signal is observed. This is very useful since it gives a zero reference reading on the tilt micrometer, which can be found during a hot run, when the electrode surface may be expected to move due to thermal expansion effects. The magnitude of this signal scattered from the electrode depends strongly on the state of the surface. With a smooth shiny surface the signal is small and difficult to detect as an increase in the reference signal due to incidental reflection and backscatter from the incident beam. However, with a rough, oxidized surface, as is certainly the case in a hot run, the reference signal increases by a factor of 2-3 and gives a good datum for determining the zero position. The detection of the zero position from the increase in reference signal is very sensitive to the setting of the scan mirror tilt micrometer, as would be expected in view of the small diameter of the focal volume. The signal peaks in a range of micrometer settings about  $\sim 0.0001$ " wide. Since the lever arm ratio is a factor  $\sim 7$ , this corresponds to a vertical deflection of the focal spot of less than  $0.001$ " or  $25 \mu$ . While this confirms that the required spatial resolution is being achieved, it also illustrates the sensitivity of the boundary layer measurements to vibration of the mirror mount and of the electrode surface during a hot run.

Calibration of the vertical deflection of the focal spot in terms of the mirror tilt micrometer was effected by placing a scale vertically across the channel and observing the deflection of the focal spot for various micrometer settings. The lever arm ratio was thus determined to be a factor 6.9.

(c) Preliminary Cold Tests

A number of performance tests were made with the system set up on a stable table in a dark room.

- (i) Focal Volume Dimensions: The diameter of the focus was determined directly by measuring the waist of the beam from the side using a high power microscope. By blowing smoke into the beam, the diameter of the waist could be observed from the scattered light to lie in the range 15-20  $\mu$ . This is a factor 2-3 greater than the calculated value, but is entirely adequate for our purpose.

The measurement of the intensity distribution along the length of the focal volume poses a difficult problem. Ideally one would like to suspend a single micron-size scatterer in the focus and measure the scattered signal as the particle is moved along the axis. Instead, we mounted a rough scattering surface normal to the beam on a translation stage, and attempted to measure the response as the surface was moved along the axis. However, because of granularity in the surface, the scattered signal was quite irreproducible. Consequently we substituted an optical flat for the rough surface. While this gave reproducible signals, it is clear that the dependence of the response to axial position is not the same for a specularly reflecting target as for a scattering one. Nevertheless, such measurements give some indications of the effective length of the focal volume.

Measurements were made in this manner with a number of different sized pinholes in the spatial filter to determine the influence of this parameter, as shown in Fig. 17. Theoretically we would expect the axial response to be sharpest for the smallest pinhole ( $4.7 \mu$ ) but in practice, better results were obtained with the largest ( $15 \mu$ ). Since the magnitude of the reference signal scattered from the edges of the pinhole could be reduced appreciably by using the largest pinhole, this was adopted as standard. The length of the focal volume to half power, measured in this way, is  $\sim 0.8$  mm, which is some five times the calculated value to half intensity points.

- (ii) Test with an Incandescent Electrode: To check that the velocimeter would allow measurements to be taken adjacent to an incandescent electrode, the beam was focused at grazing incidence on the surface of a tungsten ribbon lamp. The zero position could be found by observing the increase in the reference signal as described earlier. No change in the display was observed when the lamp was heated to  $\sim 2500^\circ\text{C}$ , which shows that there is adequate filtering against the background radiation even when the spot is focused on the electrode surface.
- (iii) Velocity Resolution: The overall velocity resolution of the system can be tested by placing a rotating disc at the focus. However, to obtain useful measurements a rather high disc speed  $\sim 100$  m/sec would be required and such a test was not made since a suitable motor-driven disc was not readily available.

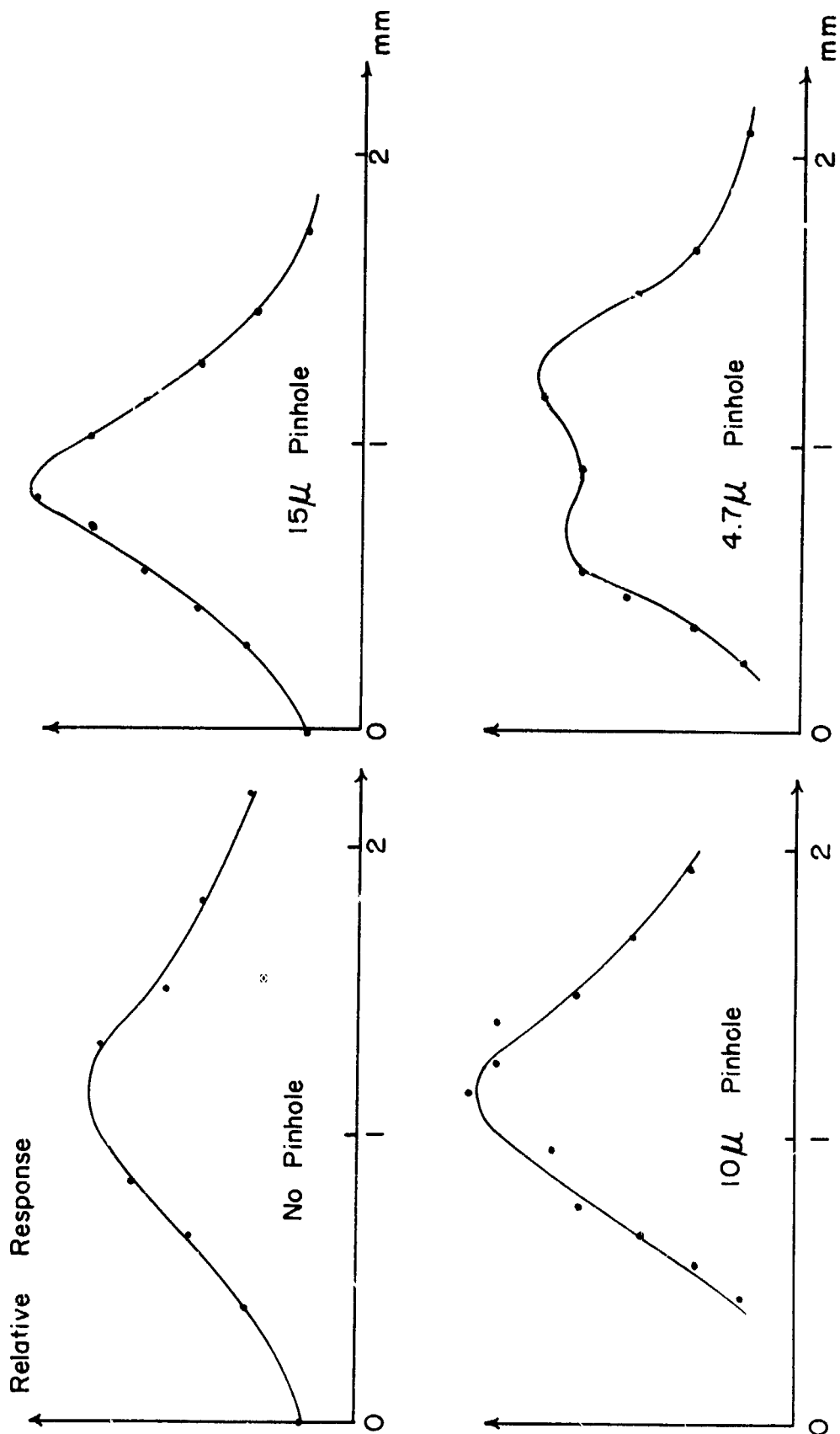


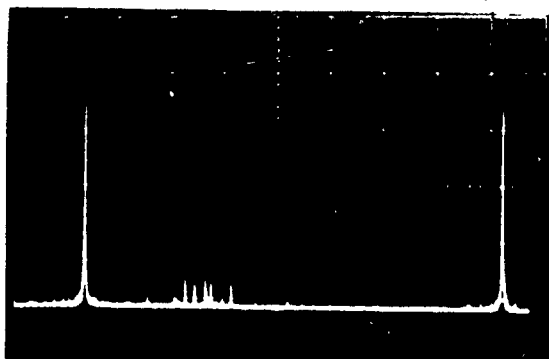
Figure 17 Influence of Pinhole Size on Response

(iv) Tests on a Water Atomizer: For these tests, use was made of a paint spray atomizer fed with water and powered by a compressed air line at 50 psi. The nozzle had a central conical needle which could be adjusted to give an extremely fine spray, such that the water consumption was less than  $1 \text{ cm}^3/\text{min}$  and the droplets evaporated within a distance of some 10 cm from the nozzle.

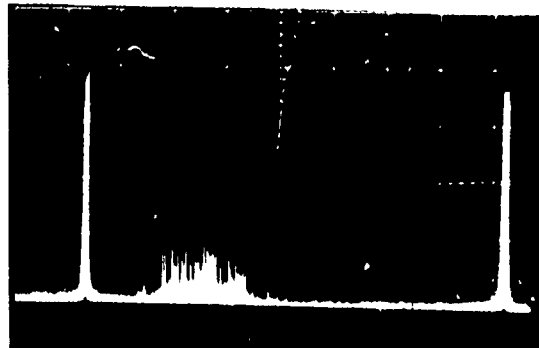
The beam was directed at an angle  $\alpha \sim 26^\circ$  to the jet axis and focused to a point about 1 mm in front of the nozzle, whereupon strong doppler shifted scattered signals were observed in the oscilloscope display as shown in Figs. 18. Signals were observed over a wide range of velocities from  $\sim 50 \text{ m/sec}$  up to a maximum of  $\sim 250 \text{ m/sec}$ , the maximum being set by the velocity of sound, since the nozzle is a choked flow. It is clear that the flow is very inhomogeneous, there being a wide range of particle size and velocity present, as well as a high degree of spatial inhomogeneity. Although the characteristics of the flow, i.e. particle concentration and size distribution, are not sufficiently known to allow a quantitative evaluation of the velocimeter, the atomizer formed a convenient source to prove the operation of the system, at least qualitatively.

The conditions for the results of Figs 18 are as follows: Scan rate  $1 \text{ msec/cm}$ ,  $v_{\text{max}} = 570 \text{ m/sec}$ , photomultiplier voltage 2000, load resistor  $10 \text{ k } \Omega$ , vertical sensitivity  $50 \text{ mV/cm}$ . Fig. 18 (a) is for a single scan (10 msec), while Figs. 18 (b) through (e) consist of  $\sim 100$  scans corresponding to a storage time  $\sim 1 \text{ sec}$ . The narrowness of the reference and scattered signals in Fig. 18 (a) shows that a velocity resolution of  $\sim 1\%$  is achieved, and also shows that the particle concentration is high enough ( $\sim 10^5 \text{ cm}^{-3}$ ) to give of the order of 5 signals per scan. The degradation in velocity resolution due to frequency jitter in the laser is evidenced by the broader reference lines in Figs. 18(b) to (e). The only difference in condi-

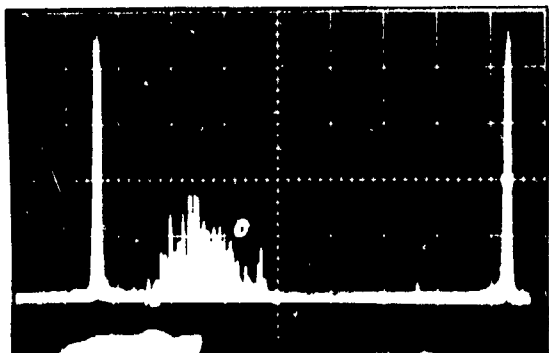
Reproduced from  
best available copy.



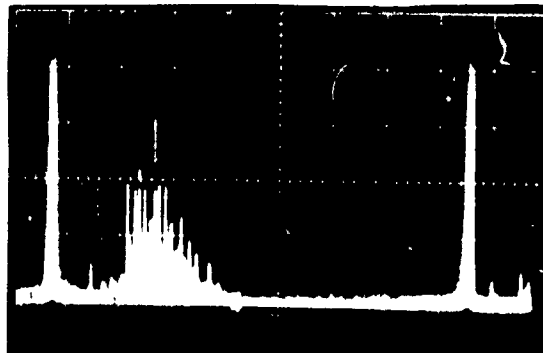
(a)



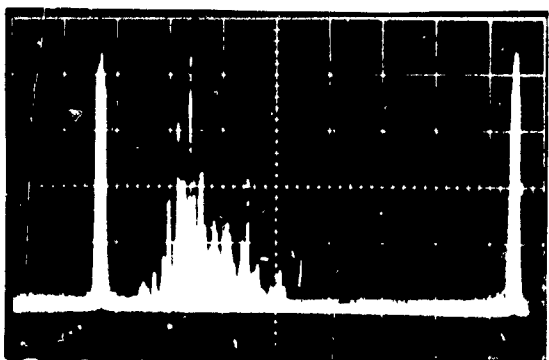
(b)



(c)



(d)



(e)

Fig. 18 Results from Cold  
Test with Water Atomiser

tions in these figures, apart from the statistical variation from shot to shot, is the setting of the intensity of the oscilloscope. This illustrates an interesting characteristic of this type of display. Since there is a wide range of particle sizes present, with more small particles than large ones, there is a corresponding range in amplitude of signals. However the pulses are all of the same length, determined by the time constant of the detector, so that the vertical writing speed for large signals is much higher than for small signals. Consequently the oscilloscope preferentially records small signals. Fig. 18(b) shows a continuum of small signals, with a number of larger signals showing separately. As the intensity is set higher, in Figs. 18(c) through (e), so the infrequent larger signals are recorded. Figs. 18(d) and (e) show an asymmetry in the size-velocity distribution, with the larger particles concentrated at lower velocities. This is to be expected since large particles will lag further behind the gas velocity in the nozzle.

It is clear that the signal to noise performance in Figs. 18 is entirely adequate. However, in the absence of any data on the size distribution of water droplets present in the atomizer jet, it is not possible to put a figure on the signal to noise performance to be expected with a given size of particle.

#### (d) First Hot Test on MHD Flow

As a first trial an attempt was made to detect signals from particles naturally present in the MHD combustion flow. No reliable information was available concerning such particles, but since the MgO firebrick walls ablate at an appreciable rate ( $\sim 1$  mm/hour), it was hoped that this might provide sufficient scattering centers. In the event no signals were de-



tected, and subsequent consideration led to the conclusion that since the vapor pressure of MgO is some 100 torr at the flow temperature (2400°C), the ablation must take place entirely by vaporization. The partial pressure of MgO near the channel wall probably reaches an appreciable fraction of this saturated value, otherwise the ablation rate would be much higher than observed. The possibility of condensation of MgO to form particles near the cooler electrode is unlikely because of the very short time available ( $10^{-4}$  secs).

Thus the result of this test was negative and we are forced to consider the addition of particles to the flow as discussed below. However some useful experience and information was obtained in other respects.

The port and window design proved adequate and no window damage was detectable after approximately one hour of running. The laser operated stably with regard to thermal tuning over the length of the run. It was also found possible to follow the movement of the electrode surface ( $\sim 0.005''$ ) due to expansion, by monitoring the position of the scan mirror micrometer to give an increase in reference signal. Some indications were also obtained concerning the severity of the problems associated with vibration induced by the turbulent flow. These are twofold. Firstly, an appreciable increase in frequency jitter in the display was observed, and is undoubtedly due to vibration communicated to the laser. This degraded the velocity resolution to some 10%, and while it does not preclude taking measurements, it is clearly undesirable. Probably the most satisfactory solution would be to mount the laser and all the optics, except the focusing lens and scan mirror on a stable platform remote from the MHD rig. Secondly it was clear the position of the focal spot relative to the electrode surface is subject to appreciable jitter, which would degrade the

spatial resolution. This could be adduced from the fact that the increase in reference signal, when the scan mirror micrometer was set to focus the beam at the electrode, was subject to jitter, and a jittering signal could be detected over a wider range ( $\sim 0.001''$ ) of the micrometer, corresponding to a jitter amplitude at the electrode of some  $0.007''$ . This may be attributed to vibration of the electrode surface and, or, vibration of the mirror mount. The main contribution is probably the latter, and this indicates the need for a more rigid mirror mount.

(e) Seeding the Flow with Particles

The principal requirements to be met by the seed material are that it should be readily available in bulk in the size range  $1-10\mu$ , and that its vapor pressure at the flow temperature should be sufficiently low that the particles do not evaporate during their time of transit ( $\sim 1$  msec) through the channel. Of the various refractory powders available, classified for size, Alumina, as prepared for grinding and polishing, appears to be the most suitable. The question of evaporation may be assessed as follows.

Assuming that the evaporation is not limited by heat transfer from the gas, so that the particle assumes the gas temperature  $T$  ( $^{\circ}\text{K}$ ), the mass evaporation rate can be written

$$E = 2.7 \times 10^{19} \left( \frac{p}{760} \right) \left( \frac{273}{T} \right) \left( \frac{mT}{2\pi} \right)^{1/2} \text{ grams/cm}^2/\text{sec} ,$$

where  $p$  (torr) is the vapor pressure,  $m$  (grams) is the molecular mass and  $k = 1.38 \times 10^{-16}$  ergs/ $^{\circ}$  is Boltzmann's constant. By evaporation the radius of a spherical particle decreases linearly with time and its lifetime can be written

$$\tau = \frac{\rho a}{E} \text{ secs} ,$$

where  $\rho$  (grams/cm<sup>3</sup>) is the density and  $a$  (cm) is the initial radius.

For Alumina, we have the molecular weight = 102 ,  $\rho = 3.7$  and at  $T = 2700^\circ\text{K}$  ,  $p = 10$  torr. We then find a lifetime  $\tau = 34a$  secs. Thus for  $1_\mu$  diameter particles the lifetime (1.7 msec) is marginal, but for particles of  $5_\mu$  diameter or more it should be adequate.

For the assumed flow conditions, the mass flow of  $\text{Al}_2\text{O}_3$  powder necessary to give a particle concentration of  $n \approx 10^3 \text{ cm}^{-3}$ , is about 0.4 grams/sec or 4 lbs/hr. There would appear to be no great difficulty in feeding powder into either the alcohol fuel or the nitrogen gas at this rate. For an initial experiment it appeared to be rather simpler to add the powder to the fuel, and a mixing system was devised for this purpose, as shown in Fig. 19. A high pressure gas cylinder was modified to contain the charge of particles and fuel, so that it could be stirred by a motor-driven paddle. The mixture is driven by the pressure (150 psi) of a nitrogen cylinder through a flow meter and mixes with the alcohol in the main fuel line. The subsidiary flow of particles and alcohol constituted a maximum of some 10% of the total fuel flow, so that the particles could be added without changing the flow condition appreciably.

(f) Second Hot Test (with seeded flow)

For this test the mixing cylinder was charged with 10 gallons of alcohol and 10 lbs of Alumina powder of a nominal 5 micron size. At the

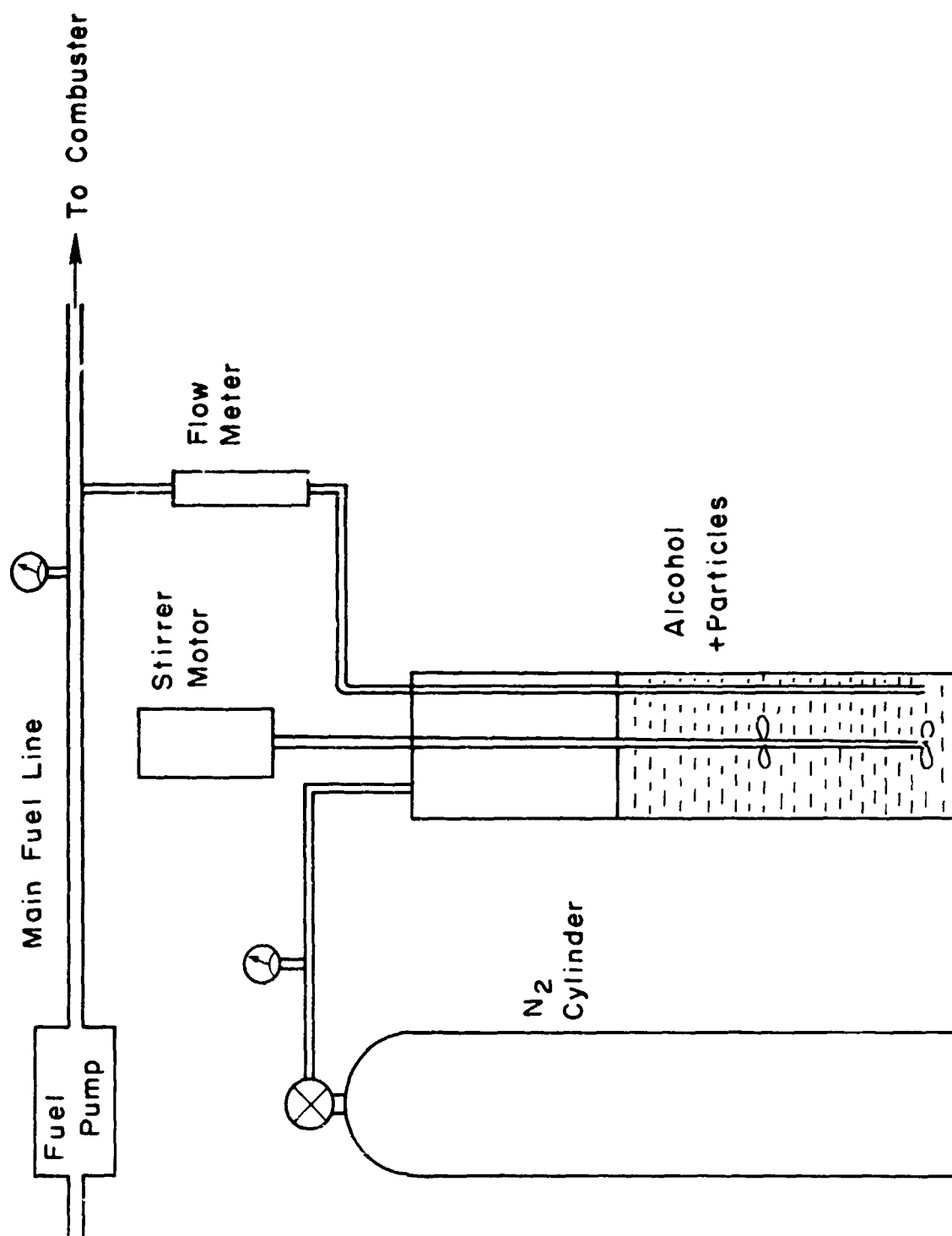


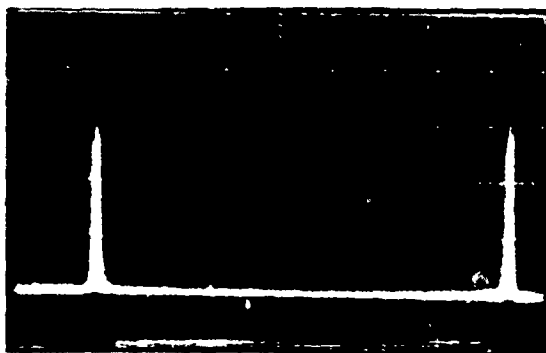
Figure 19 Particle Mixing and Injection System

maximum flow rate of  $\sim 0.22$  gal /min ( $\sim 0.025$  lbs/sec Alcohol) indicated by the flow-meter, the particle feed system would run for approximately an hour. For a channel flow velocity of  $\sim 500$  m/sec, this gives a calculated particle concentration of  $\sim 10^3 \text{ cm}^{-3}$ , which should give a detected signal acquisition rate of a few per second.

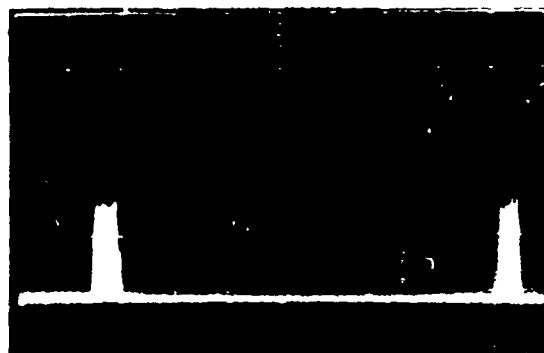
Fig. 20(a) shows the reference signals in the velocimeter display before starting the hot flow. Figs. 20 (b) and (c) show the display after warm up, with the flow conditions set to give a free stream velocity of  $\sim 500$  m/sec at a temperature of  $\sim 2400^\circ\text{C}$ . Fig. 20(b) is with the detector sensitivity set the same as in Fig. 20(a) while in Fig. 20(c), the amplified gain has been increased by a factor  $\sim 10$  to show the noise level. These figures show, from the width of the reference pulses, the degradation of velocity resolution due to the frequency jitter induced by the vibration coupled from the M.H.D. channel to the laser.

After the flow had become steady, the particle feed was activated and attempts made to record signals due to particles. However no positive results were obtained, and it was thought that perhaps the particles were being evaporated before reaching the measurement point. Accordingly the nitrogen feed to the channel was increased to reduce the flow temperature somewhat (to approximately  $2250^\circ\text{C}$ ), but still no signals were seen. At this stage it was decided to try adding more powder to the mixing cylinder which, by this time was approximately half full. Since no more Alumina was at hand, 5 lbs of fly ash graded between 5 and 10 micron was added, but still no unambiguous signals were detected.

At this point it was thought that, since the nominal flow velocity was 500 m/sec, while the free spectral range of the Fabry-Perot was 572 m/sec,



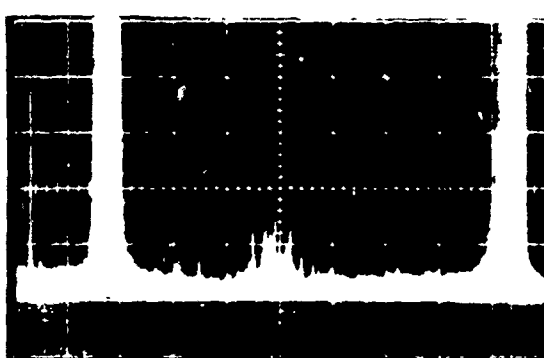
(a)



(b)

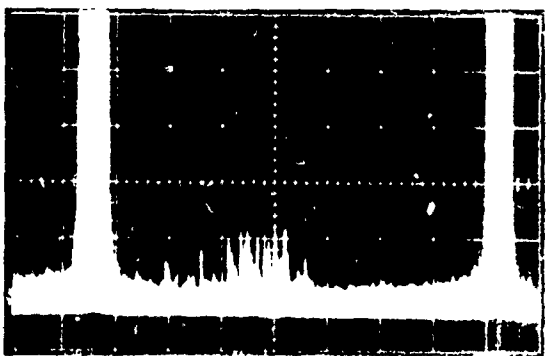


(c)



(d)

Reproduced from  
best available copy.



(e)

Fig. 20. Results from Hot  
Test with  $\mu$  Alumina particles.

the signals were being masked behind the broadened reference signals. Accordingly the fuel, Oxygen and Nitrogen feed rates to the channel were reduced to give a free-stream velocity of some 250 m/sec. Immediately, doppler shifted signals were seen as shown in Figs. 20(d) and (e). These were taken with the same detector sensitivity as for Fig. 20(c) and correspond to storage times of 5 ~ 10  $\mu$ sec. The distance of the focal spot from the electrode surface was 10.4 and 6.0 mm respectively for these results, and both give average velocities of  $240 \pm 10$  m/sec, which agrees well with the calculated free stream velocity (250m/sec).

Some comments on these results may be made as follows. The apparent velocity spread is quite large, but the actual velocity spread present in the flow is smaller, being artificially broadened as a result of the frequency jitter due to vibration. The amplitude of the signals is only a few times the noise level. It should be noted that reducing the flow velocity to one half has the effect of increasing the scattered pulse length and hence the detected pulse amplitude by a factor of two. The acquisition rate of detected signals was also lower than expected. Both the smallness and the infrequency of the signals may be explained by the subsequent observation that little of the particulate matter was reaching the measurement point.

Following these measurements in the free stream, measurements were begun in the boundary layer. However, at this stage the run was terminated due to the appearance of large and destructive lumps of solid in the flow. Subsequent examination revealed that a considerable fraction of the particulate matter had condensed as slag on the cold wall of the combustor and was becoming detached and projected along the channel. It appears

that the particles were melted and probably vaporized in the flame. The centrifugal action of the oxygen feed then threw this out to the cold walls where it condensed. Unfortunately, because of the sequence of operations, it is not clear whether this was due to the Alumina or the fly ash or both. However, we might expect that the fly ash contributed largely to this since its composition is approximately 50%  $\text{SiO}_2$ , 25%  $\text{Al}_2\text{O}_3$  and 25%  $\text{Fe}_2\text{O}_3$  by weight, and silica boils at  $\sim 2200^\circ\text{C}$ .

Although the addition of particles to the fuel allowed us to obtain some preliminary results, it is clear that it will be necessary to inject the particles into the nitrogen, further downstream, where they will not be exposed to the high flame temperature or the cold walls of the combustor.

#### 4.2.6 Summary and Conclusions

Following a detailed design study, a laser doppler velocimeter has been constructed for measuring the gasdynamic boundary layer velocity profile adjacent to an electrode in the Stanford combustion MHD facility. Preliminary tests indicate that the design requirements with respect to spatial resolution ( $\leq 0.1$  mm), velocity resolution ( $\leq 2\%$  of free-stream value) and signal detectability (for  $5\mu$  particles) can be met.

In the first hot run, no scattered signals were detected and it was concluded that it will be necessary to seed the flow with suitable particles. In a second hot run, seed particles were added to the alcohol fuel. At a flow velocity of 500 m/sec no unambiguous signals were observed. This is attributed to the fact that they were only marginally above noise and masked by the broadened reference signal at 570 m/sec.



When the velocity was reduced to 250 m/sec, clear signals, several times the noise level were obtained. The velocity deduced from these agreed with the free stream velocity calculated from the known flow conditions to within the experimental error. The test was terminated as a result of problems associated with the formation of slag from the particulate matter in the combustor section.

While these results are encouraging and demonstrate the method in principle, it is clear that considerable further development will be necessary in a number of areas, before the technique can be reliably used to measure velocity profiles with the required accuracy. The aspects in which the performance must be improved are primarily (i) enhancement of signal to noise performance and reduction of the reference signal amplitude, (ii) improvement in the frequency stability of the laser, (iii) reduction of vibration of the focal spot position relative to the electrode surface. Furthermore a suitable method of feeding seed particles into the gas flow, upstream of the measurement point, must be developed. There is every reason to believe that these requirements can be met and the laser doppler velocimeter developed into a precise instrument for the measurement of boundary layer velocity profiles in MHD channels.

## 5.0 Summary

The research program supported under contract AF F33615-69-C1171 has dealt with boundary layer studies, with current distribution and leakage studies and with boundary layer diagnostics. In the first area a computer program has been written which couples the MHD generator core flow and the turbulent boundary layer. The program yields the local heat transfer coefficient and shear stress as well as profiles of velocity and temperature. Measurements in an argon flow showed the extreme sensitivity of the electrode voltage drop to small concentrations of  $\text{CO}_2$  and  $\text{N}_2$ . An extension of this work will lead to a better understanding of the surface-sheath component of the voltage drop which has not yet been studied in detail. The influence of the boundary layer temperature and electrode temperature on electrode voltage losses for several electrode sizes was studied. It was shown that under some conditions small electrodes had less voltage drop than large electrodes. Designers must consider temperatures and spacing of both insulators and electrodes in optimizing electrode designs.

The current pattern in a conducting-wall generator showed considerable current collected by the side walls. It was also shown that Faraday generator electrodes which extended up the side walls resulted in more power than conventional flat electrodes. A calculation of current patterns showed good agreement with experimental data at the anode but power agreement at the cathode where surface-sheath voltage drops are greater.

A new method which uses Faraday splitting of laser modes is suggested for the measurement of electron concentration in the boundary layer. A laser doppler velocimeter and its application to boundary layer velocity measurements is described.

## REFERENCES

- [1] Pantankar, S. V. and D. B. Spalding, Heat and Mass Transfer in Boundary Layers, Morgan-Grampian, London (1967).
- [2] Kays, W. M., Moffat, R. J., and Thielbahr, W. H., "Heat Transfer to the Highly Accelerated Turbulent Boundary Layer With and Without Mass Addition," 1969. HMT 6, Mechanical Engineering Department, Stanford University.
- [3] Kessler, R., "Effects of Electrode Temperature on MHD Generator Performance," SU-IPR Report 239, June 1968.
- [4] Cutting, John C., "Axial Current Leakage in Segmented MHD Generators," SU-IPR Report 406, January 1971.
- [5] Johnson, W. B., IEEE Trans. On Antennas and Propagation, AP-15, 152 (1967).
- [6] Turner, R. and Poehler, T. O., J. Appl. Phys., 39, 5726 (1968)
- [7] Chamberlain, J., Gebbie, H. A., George, A. and Beynon, J. D. E., J. Plasma Phys., 3, 75 (1969).
- [8] Olsen, J. N., Rev. Sci. Instr., 42, 104 (1971).
- [9] Johnson, W. B. Larsen, A. B. and Sosnowski, T. P., Proc. 7th International Conference on Ionization Phenomena in Gases, 1966, Vol. 3, p. 220.
- [10] Aronowitz, F. and Collins, R. J., Appl. Phys. Letters, 9, 55 (1966).
- [11] Tomlinson, W. J. and Fork, R. L., Phys. Rev., 164, 466 (1967).